



HAL
open science

Geomagnetic field variations between chrons 33r and 19r (83-41 Ma) from sea-surface magnetic anomaly profiles

Claire Bouligand, Jérôme Dymont, Yves Gallet, Gauthier Hulot

► To cite this version:

Claire Bouligand, Jérôme Dymont, Yves Gallet, Gauthier Hulot. Geomagnetic field variations between chrons 33r and 19r (83-41 Ma) from sea-surface magnetic anomaly profiles. *Earth and Planetary Science Letters*, 2006, 250 (3-4), pp.541 - 560. 10.1016/j.epsl.2006.06.051 . hal-01812932

HAL Id: hal-01812932

<https://hal.science/hal-01812932>

Submitted on 12 Jun 2018

HAL is a multi-disciplinary open access archive for the deposit and dissemination of scientific research documents, whether they are published or not. The documents may come from teaching and research institutions in France or abroad, or from public or private research centers.

L'archive ouverte pluridisciplinaire **HAL**, est destinée au dépôt et à la diffusion de documents scientifiques de niveau recherche, publiés ou non, émanant des établissements d'enseignement et de recherche français ou étrangers, des laboratoires publics ou privés.

Geomagnetic field variations between chrons 33r and 19r (83-41 Ma) from sea-surface magnetic anomaly profiles

C. Bouligand^{*}, J. Dyment, Y. Gallet, G. Hulot

Institut de Physique du Globe de Paris (Institut de recherche associé au CNRS et à l'Université Paris 7), 4 place Jussieu, 75005 Paris, France

Submitted to *Earth Planet. Sci. Lett.*, April 6, 2006, revised June 15, 2006.

Abstract

Sea-surface magnetic profiles exhibit coherent short wavelength "micro-anomalies" (or "tiny wiggles") superimposed to the main anomalies due to reversals. In this study, we investigate the nature and distribution of these tiny wiggles on oceanic crust formed during the ~ 42 Myr-long period following the Cretaceous Normal Superchron. To this end, we compute stacks of anomaly profiles from different areas in the Indian and Pacific oceans. Using a simple method based on upward continuation, we demonstrate that, the tiny wiggles are consistent worldwide although their patterns exhibit different resolutions at different spreading rates. They are therefore confidently ascribed to past fluctuations of the geomagnetic dipole moment. A high resolution record of these fluctuations is obtained by selecting and stacking profiles from areas with the highest spreading rates. Modeling the micro-anomalies as short magnetic polarity intervals yields durations for these intervals generally shorter than 10 kyr, likely too short to be indeed "true" subchrons. Moreover, the number of detected tiny wiggles clearly depends on the spreading rate. These results support geomagnetic intensity fluctuations as being the cause of most tiny wiggles, as also

suggested by recent magnetostratigraphic data. The tiny wiggles are uniformly distributed within chrons, indicating that paleointensity fluctuations are neither inhibited after, nor enhanced before, a reversal beyond a "blind" zone of about 10 km (corresponding to 80 to 250 kyr depending on the spreading rate) for which the anomalies due to reversals prevent the detection of tiny wiggles. Most tiny wiggles probably represent a filtered record of a uniform secular variation regime, as suggested by their uniform spatial distribution over the whole investigated period.

Key words: marine magnetic anomalies, tiny wiggles, paleosecular variation, paleointensity, Late Cretaceous - Cenozoic

1 Introduction

The analysis of sea-surface magnetic anomaly profiles has revealed many coherent micro-anomalies in addition to the major anomalies linked to reversals (e.g. [1–6]). The correlation of these micro-anomalies, or "tiny wiggles", among distant oceanic basins demonstrate that most of them are related to paleo-variations of the Earth's magnetic field and not to local magnetic sources in the oceanic crust [7,6]. Although often modeled as short magnetic polarity intervals (the so-called "cryptochrons" of Cande and Kent [7,6]), they may in fact be due to strong geomagnetic field intensity variations such as those occurring during excursions [8–10]. Up to now, the detection of tiny wiggles has been performed over only a limited number of short intervals and has often been based on favorable profiles from one ocean basin, occasionally complemented by a limited set of profiles from other oceans [3,6]. In this study, we conduct an extensive investigation of the occurrence and distribution of tiny wiggles over a long period, namely between chrons 33r and 19r (83-41 Ma), from profiles obtained in the Indian, North and South Pacific oceans, characterized by fast spreading rates at that time. A

* Corresponding author. Tel.: 33 1 4427 2407; fax: 33 1 4427 3777.

Email addresses: bouligan@ipgp.jussieu.fr (C. Bouligand), jdy@ipgp.jussieu.fr (J. Dyment), gallet@ipgp.jussieu.fr (Y. Gallet), gh@ipgp.jussieu.fr (G. Hulot).

large number of scalar sea-surface magnetic anomaly profiles are used to compute regional stacks in the different studied areas. Selecting areas displaying the fastest local spreading rates, we finally compute a composite high resolution stack. This work provides new constraints on the distribution of tiny wiggles during a period characterized by a low to moderate magnetic reversal frequency and offers the possibility to make comparisons with the recent period for which the magnetic reversal frequency is high and the geomagnetic excursion distribution rather well known [10].

2 Data

The data used in this study are sea-surface total-field magnetic profiles extracted from two databases: the Marine Trackline Geophysics Database compiled by the U.S. National Geophysical Data Center (<http://www.ngdc.noaa.gov/mgg/fliers/03mgg02.html>) and a French database for the Indian Ocean (http://barkeria.u-strasbg.fr/archivage/diffu_indien.html).

We use the magnetic lineation map of Cande et al. [11] as a guideline to select areas with a simple tectonic context (parallel magnetic lineations over wide areas) and relatively fast spreading rate (Figure 1). In each investigated area, only profiles crossing the magnetic lineations with a maximum angle of 45° from the spreading direction are selected (Figure 1). We reject parts of profiles crossing major transform faults, identified seamounts or any other significant structural perturbations in the topography as depicted in the free-air gravity anomaly map [12]. We also reject profiles showing no clear magnetic anomaly sequence or too sparsely sampled.

Five areas are selected in the Indian Ocean. The Central Indian Ridge (CIR) and the South East Indian Ridge (SEIR) underwent an important decrease of the spreading rate followed by a major reorganization in spreading orientation between anomalies 22 and 18, i.e. 49-38 Ma [13,14]. The selected areas correspond to oceanic crust produced before these major modifications. Conjugate areas produced at the CIR axis are the western part of Central Indian Basin (area 2) and the Madagascar Basin (area

4); conjugate areas produced at the SEIR axis are the eastern part of Central Indian Basin (area 1) and the Crozet Basin (area 3). Western and eastern parts of the Central Indian Basin are separated by the Indian triple junction trace [14]. The fifth area (area 5), in the Wharton Basin, was formed on the southern flank of a fossil ridge which separated the Indian and Australian Plates and was connected to the western part of the SEIR before the major change of spreading configuration at anomalies 18-22. The spreading direction is north-south in these five areas, so the anomaly amplitude is large (± 400 nT). The total amount of data selected in the Indian Ocean includes 160 profiles collected during 71 cruises.

Five areas are selected in the North Pacific Ocean (Figure 1). In these areas, the tectonic is rather simple: major transform faults limit lithospheric compartments which have been formed along a westward spreading direction. In the northern end, the spreading direction changes and becomes oriented southward. We select one area with southward spreading direction (area 6 located south of the Aleutian Subduction Zone and north of the Chinook Trough) and four areas with westward spreading direction. The latter four areas are limited by transform faults (from north to south): area 7 north of the Mendocino Fracture Zone (FZ), area 8 between Mendocino and Murray FZ, area 9 between Murray and Molokai FZ and area 10 between Molokai and Clarion FZ. As the spreading direction in these four areas is oriented east-west, the amplitude of the observed anomalies decreases close to the magnetic equator (from ± 350 nT on area 7 at latitude $\sim 45^\circ\text{N}$ to ± 100 nT on area 10 at latitude $\sim 20^\circ\text{N}$). The signal to noise ratio thus also decreases close to the Equator, in particular in area 10 where the major anomalies due to reversals are more difficult to recognize than in the other areas. Area 6 is characterized by large anomaly amplitudes (± 500 nT). Many data are available in this area. However most of them have been acquired before 1970. For this reason, the overall quality of these records is rather poor and the sampling interval is often large (the majority of the profiles are sampled with intervals larger than 2 km). The total amount of data selected in the North Pacific Ocean includes 325 profiles collected during 102 cruises.

Six areas are selected in the South Pacific Ocean (Figure 1). The spreading history of this ocean is complex and only few data are available. Nevertheless, some of those profiles are very interesting

because of a very fast local spreading rate [15]. Areas 11 to 13 are located on the Pacific Plate and areas 14 to 16 on the Antarctic plate. The Pacific-Antarctic Ridge produced areas 11 (south of FZ 8.5, see the location of the FZ in McAdoo and Laxon [16]) and 12 (north of FZ 8.5 and south of Heezen FZ) on its western flank, and area 14 (south of Heezen FZ) on its eastern flank. Area 15 (north of FZ V and south of Humbolt FZ) is the young extension of area 13 (north of Heezen FZ). They were both produced on the Pacific Plate, on the western flank of the Pacific-Aluk Ridge, but were later separated by a ridge jump, area 15 being transferred to the Antarctic Plate [15]. Areas 13 and 15 are characterized by a very fast spreading rate, about 80 km/Ma [6,15]. Area 16 (north of Heezen FZ and south of FZ V) was produced on the north-western flank of the Aluk-Antarctic Ridge [15]. The anomaly amplitude in all these areas is relatively large (± 300 nT). The total amount of data selected in the South Pacific Ocean includes 89 profiles collected from 36 cruises.

3 Profile analysis

First of all, we compute the scalar magnetic anomaly by correcting the magnetic measurement for the strength of the main field calculated up to the degree 10. The Gauss coefficients of the main field are interpolated between the coefficients given by the International Geomagnetic Reference Field (IGRF) models [17] calculated every five years. The coordinates of the profiles are projected along the spreading direction (Table 1). Each profile is resampled at a constant interval equal to the mean sampling interval. All individual profiles are reduced to the pole in order to allow for comparisons among profiles obtained from distant areas. To this end, we correct the magnetic profiles for the skewness. But we do not correct the amplitude effect to keep the noise at a comparable level on all profiles. The correction is obtained by applying the inverse phase filter $\exp(i\theta)$ [18]. The skewness is determined visually by searching for the best angle θ so that the corrected profile resembles the anomaly model computed to the pole with the algorithm of Talwani and Heirtzler [19] using the Cande and Kent [20] magnetic polarity time scale. Although the skewness angle varies both in space and time (because of the varying regional field and magnetization directions), we assume here that

these variations remain small enough within the different areas, and we apply the same angle θ to all profiles from each area (Table 1). This method amounts to a reduction to the pole, as the anomalous skewness first evidenced by Cande and Kent [21] is negligible for fast spreading rates [22,23].

On each profile, the reversals are precisely located by picking the inflection points of the magnetic anomaly (i.e. the extrema of the derivative of the magnetic anomaly). The distances between reversals are transformed into time using the polarity timescale established by Cande and Kent [20], assuming a constant spreading rate between two successive reversals. Finally, the profiles from a given area are resampled with the same time interval (10 kyr) and stacked.

4 Regional stacks and spreading rates in the different areas

We carefully examine all profiles from each area and eliminate those which seem suspicious because they display micro-anomalies with different length-scales or larger amplitudes than the neighboring profiles. The latter may have been affected by instrumental noise or perturbation due to anomalous topography or structural features. Before computing a "final" regional stack and picking the micro-anomalies, we check that the pattern of tiny wiggles can be recognized in most profiles from one area. To this end, the influence of individual profiles is tested by recomputing a stack after removing one of the profiles and checking the stack variability. The profiles which introduce micro-anomalies in one stack that are not present in the others are eliminated except if the total number of available profiles is small (i.e. less than three profiles) or if the richer content of these profiles can be explained by a locally faster spreading rate.

All computed regional stacks are presented in Figure 2. One may notice a residual skewness in some stacks, especially for older (chrons 32n to 33r) and younger (chrons 19r to 20r) ages, which reflects the fact that all profiles from a given area were deskewed with the same angle θ . The stacks display many short wavelength anomalies, positive or negative. As in Cande and Kent [6], we define micro-anomalies (or tiny wiggles) as negative (positive) short wavelength anomalies in normal (reverse)

polarity chrons and locate their center (blue ticks on Figure 2). The mean spreading rate variations computed for all studied areas are presented in Figure 3. The real spreading rate fluctuations within each area are likely smoother, the steps in the curves being artifacts due to the assumption of a constant spreading rate between reversals. Sharp spreading rate variations (and large relative uncertainties on the measured distances) coincide with the shortest chrons (see for instance chron 30r at about 68 Ma). More generally, some spreading rate variations are correlated among different basins and oceans (see for instance chrons 32n to 33n, 71-79 Ma) and likely reflect uncertainties in the reversal time-scale [20]. Figures 2 and 3 show that the density of tiny wiggles observed in each basin strongly depends on the spreading rate. In the Indian Ocean, the density of tiny wiggles is the highest between chrons 31n and 22r (i.e. 69-50 Ma), a period of very fast spreading corresponding to the northward motion of India. Similarly, a high density of tiny wiggles and faster spreading rate are observed in the North Pacific Ocean between chrons 21n and 19r (i.e. 48-41 Ma). The tectonic context in the South Pacific Ocean is more complex and the spreading rates are geographically variable. Area 13 and 15 are characterized by a very fast spreading rate and reveal a very detailed tiny wiggle content.

5 Comparison between the different regional stacks

To test the consistency between different regional stacks and identify a reliable sequence of micro-anomalies, we start with a simple technique. To compare two profiles (or stack profiles) from areas with different spreading rates, we simply apply an upward continuation of height Δh to the fastest profile. This height Δh was chosen in the following way. If V_1 and V_2 are respectively the slow and fast spreading rates and h_1 is the initial water depth (identical for seafloors of same age, e.g. [24]), Δh is such that:

$$\frac{V_2}{V_1} = \frac{h_1 + \Delta h}{h_1} \quad \text{i.e.,} \quad \Delta h = h_1 \left(\frac{V_2}{V_1} - 1 \right) \quad (1)$$

For the anomalies considered in this study, h_1 ranges from about 4750 m to about 5550 m (according to Parsons and Sclater [24]). In practice, we used $h_1 = 5000$ m.

Indeed, if the magnetization pattern is identical in the two systems with different spreading rates, the geometry of the slow spreading system is almost a scaled down version of that of the upward-continued fast spreading system, and the resulting magnetic profiles are therefore very similar. They would be strictly identical if the magnetized layer at fast spreading rate was thicker by a factor V_2/V_1 . The classical assumption of a constant thickness for the magnetized layer affects the amplitude of the anomalies but also, to a lesser extent, the shape of the power spectrum. However, modeling anomaly profiles with different realistic spreading rates shows that our technique introduces only minor differences between the slow and upward-continued fast spreading rate profiles, which are negligible for the purpose of this study. Downward-continuing the slow spreading rate profiles to compare them with faster spreading rate profiles was not an option, as it increases the noise level and would prevent the accurate detection of the tiny wiggles.

For each chron, we select the stack from the area characterized by the fastest spreading rate and upward-continue it for comparison with the stacks from areas with slower spreading rates (Figure 4). Three different types of areas are considered: 1) areas with fast spreading rates where a detailed pattern of tiny wiggles can be recovered; 2) areas with intermediate spreading rates which give a magnetic signal smoother than the previous ones, but can still be used to test the consistency of records from faster spreading rate areas; 3) areas with slow spreading rates, where the magnetic records do not have enough resolution to display any micro-anomaly. A general description of the regional stacks is summarized in Table 2. Below we only describe a few selected chrons in detail.

Chron 20r The spreading rate is much faster in the North Pacific than in the Indian and South Pacific oceans, characterized by smoother stacks. In the North Pacific Ocean, the spreading rate decreases from South to North (Figure 3b), so the computed stacks are smoother from South to North (areas 10 to 7). Areas 10 and 9 show the highest resolution. However, as previously stated, the anomaly amplitude is low in area 10 (± 100 nT) and the resulting stack may therefore be noisier. The general shape of the stacks from areas 7 to 10 exhibits a very nice correlation: the five bumps of the smooth area 7 are recognized with finer details in the three other areas. With increasing spreading rate, the

bump at 44.3 Ma splits into three tiny wiggles (a, b, and c, areas 9 and 10), the one at 45 Ma into two tiny wiggles (e and f, areas 8 and 9) and those at 45.6 and 45.8 Ma become three tiny wiggles (g, h, and i, area 8 and 9). The upward continued profiles obtained from the stack of area 9 are consistent with the stacks of other areas, including areas from Indian and South Pacific oceans, except for area 5 characterized by a very smooth anomaly. Nine tiny wiggles (a - i) are identified for this period.

Chron 23r Three tiny wiggles (a - c) are recognized in all stacks from the Indian Ocean (areas 1 to 5), characterized by a faster spreading rate. The upward-continued stack from area 1 is consistent with those from the other areas.

Chron 24r A good correlation exists between the stacks from different areas in the Indian Ocean, especially areas 2, 4 and 5 which include a larger number of profiles. The upward-continued stack from area 4 is consistent with all but two stacks from the other areas. In area 6, located close to the Aleutian Subduction Zone in the North Pacific Ocean, chron 24r is recorded with a very fast spreading rate, comparable to the one found in the Indian Ocean; however the stack in area 6 is much smoother than it should be according to its spreading rate. This may be due to the wide sampling interval of the old magnetic anomaly profiles available in this region. Despite its lower resolution, this stack displays the three large bumps that are recognized in areas with slower spreading rate. The stack from area 15 correlates well with the upper-continued one from area 4 if we allow for a quite significant shift of the anomalies, which probably reflects large spreading rate variations during this period in this area. Ten tiny wiggles (a - j) are finally recognized.

For chrons 25r and 26r, area 15 in the South Pacific Ocean is characterized by a faster spreading rate than areas in the Indian Ocean but includes only a few profiles. For this reason, two figures present the upward-continued stacks from area 5 in the Indian Ocean and from area 15 in the South Pacific, respectively.

Chron 25r A good correlation is observed between stacks from the Indian Ocean. The upward-continued stack from area 15 in the South Pacific Ocean is not consistent with the shape of the stacks of other areas; the spreading rate is very fast for chron 25r (about 120 km/Myr) compared to the

previous and following chrons 24r and 26r (about 70 km/Myr), a quite suspicious observation that may reflect some local tectonic complexity (a ridge jump?). The upward-continued stacks from area 5 are consistent with the stacks of other areas. Five clear tiny wiggles (a, b and d - f) and possibly a sixth one (c) are found.

Chron 26r The stacks from the Indian Ocean correlate well. The upward-continued stack from area 15 in the South Pacific is consistent with stacks from all other areas, except for the young part of the chron (58 - 58.5 Ma) which may be affected by a tectonic complication. Variations in the shape of the stacks are observed in the North and South Pacific where the spreading rate is rather slow. It may be due to irregular spreading in a slow spreading rate context. Eight clear tiny wiggles (a - h) and possibly a ninth one (i) are recognized in area 1, 2, 3 and 5.

Chron 30n Nice correlations are found between the stacks from areas 3, 5 and 13 and the one from area 1, which is smoother because it has been computed with more profiles (9 profiles compared to 3, 2, and 2 profiles for areas 3, 5, and 13, respectively). A relatively large positive anomaly is recognized around the middle of the chron. In area 3, this anomaly (noted A, between c and d) is shifted, maybe because of an irregular spreading rate. The upward-continued stack from area 13 is consistent with the others areas. Six tiny wiggles (a - f) are obtained in areas 1, 3, 5 and 13.

Chron 31r Although the different regional stacks display quite different shapes, the upward-continued stack from area 13 is rather consistent with those from all areas except areas 6 and 8 which show no micro-anomaly. The stack from area 6 includes profiles with highly variable, strong amplitude micro-anomaly patterns, which suggests a local tectonic complexity. However, some individual profiles show similarities with the stack from area 13. The stack from area 8 includes profiles with low amplitude micro-anomalies. The clearest tiny wiggle is the first bump (a) recognized in all but areas 5, 6 and 8. Seven tiny wiggles (a - g) are recognized in areas 1, 5 and 13.

Chron 33n In the Indian Ocean, only one profile is available in areas 3 and 5. These two profiles correlate very well. However, it should be mentioned that areas 3 and 5 were close to each other, on the southern flank of the Southeast Indian Ridge prior the major change in spreading configuration

at anomalies 18 and 22, and may have shared the same spreading history. The stack from area 1 includes only two profiles (many other profiles are noisy or suspicious). This stack is smoother than the profiles from areas 3 and 5; however some micro-anomalies are recognized, in particular two tiny wiggles (B and C) that are used in a later section as secondary tie-points to improve the stacks. In the North Pacific, areas 8 and 9 show many correlated micro-anomalies. Some correlations are also possible with area 10 (which includes only one profile). In these three areas, we identify micro-anomalies B and C as defined above. Area 7 includes only 3 profiles which are very different from each other and therefore suspicious. In the South Pacific, several micro-anomalies are also identified (including B and C), in particular in area 13 characterized by a very fast spreading rate. The upward-continued stack from area 13 is consistent with stacks from all areas. Good correlations are observed with areas 3, 5, 8 and 9. Twelve tiny wiggles (a - i, B, and C) are finally obtained.

Chron 33r Area 13 in the South Pacific is characterized by a very fast spreading rate but includes only one profile. For these reasons, we present two figures comparing stacks from various areas with the upward-continued stacks from areas 8 and 13. The stacks from most areas reveal two major bumps (a and b), and some profiles from different areas present local similarities. Despite the poor similarities of the stacks from various areas with the upward-continued stack from area 13, acceptable correlations between the upward-continued stack from area 8 and the other areas are observed for the longer wavelengths variations.

The stacks obtained for chrons 20n and 20r in the North Pacific are very precisely correlated among each others even though the spreading rate varies progressively from area 10 to 7. This is likely due to the fast and very regular spreading rate and the large amount of available data which are favorable conditions for a high quality record in the North Pacific during chron 20n and 20r. In contrast, correlations are not so good for chrons 24r-26r in the Indian Ocean or for chron 33n worldwide. But, areas in the Indian Ocean, where chrons 24r to 26r are recorded with a very fast spreading rate, are affected by long-offset fracture zones and the number of adequately long profiles is limited. Finally, the spreading rate is slower during chron 33n in all areas and the quality of the geomagnetic record is

therefore not surprisingly poorer. More generally, we note that the spreading rate is certainly not the only parameter controlling the quality of the geomagnetic field recorded by the oceanic crust. The amplitude of the anomalies compared to that of the noise level is also an important factor which is controlled by geographic and geological parameters, such as the latitude and the orientation of the magnetic lineations, or the structure and magnetic properties of the oceanic crust, hence the conditions of its formation at the ridge axis and its alteration on the ridge flank. Given these limitations, the stacks from different areas appear to be remarkably consistent.

6 Constructing a global high-resolution stack

The comparison between the different regional stacks reveals the occurrence of many micro-anomalies. Because they are quite consistent worldwide, these micro-anomalies can be ascribed to past fluctuations of the geomagnetic dipole moment. The overall good consistency observed between the different stacks further supports the computation of a composite, high resolution tiny wiggles record by stacking selected profiles from the areas displaying the highest spreading rates (Figure 3).

To this end, we select the following areas:

- for chrons 19r to 21r (41-49 Ma), areas 8, 9 and 10 from the North Pacific Ocean;
- for chrons 22n to 29r (49-66 Ma), areas from the Indian Ocean (except area 4 for chron 27r and areas 1 and 4 and for chron 29n, which display a slower spreading rate); and
- for chrons 30n to 33r (66-83 Ma), the best individual profiles (i.e. with the fastest spreading rates and the highest anomaly amplitudes) from all investigated oceans since the spreading rates are rather slow in almost all oceans.

For chron 33r, only the longer wavelengths (i.e. tiny wiggles a and b, in Figure 4) are consistent within regional stacks. However, several individual profiles display consistent shorter wavelengths; we therefore select these profiles to compute the high resolution stack and tentatively identify several additional tiny wiggles. Because these tiny wiggles are not observed in the regional stacks, we

consider them as less reliable.

In the case of long chrons, the hypothesis of a constant spreading rate is most likely incorrect. To improve the quality of the stacks, we introduce secondary tie points. Such a procedure is potentially dangerous, as it may artificially reinforce correlations between distant profiles. For this reason, we only consider three well-recognized anomaly patterns: tie point A within chron 30n, and tie points B and C within chron 33n. No secondary tie-point is considered within the long chron 33r. As already noted tie point A is a positive anomaly within a normal chron; however its very characteristic shape makes it the best candidate. Figure 5 indeed shows that introducing secondary tie-points B and C does not drastically modify the stacks within chron 33n for each area (compare with Figure 2 without secondary tie-points). However it does reinforce the tiny wiggles in the global stack, suggesting that their poor adjustment in our original global stack is indeed due to spreading-rate variations.

The age estimate for each secondary tie-point is derived from the median value of the age interpolated between the two bounding reversals for each stack profiles. The uncertainty is given by the standard deviation. These estimates are indicated below (with the number of profiles used for the computations):

- A (chron 30n) $t = 66.642 \pm 0.079$ Ma (14 profiles)
- B (chron 33n) $t = 75.493 \pm 0.162$ Ma (55 profiles)
- C (chron 33n) $t = 76.994 \pm 0.205$ Ma (55 profiles)

The standard deviation for point A is small because we only use the 14 profiles displaying the highest spreading rates, whereas the standard deviations for points B and C are larger because we use profiles with a larger range of spreading rates.

Figure 6 shows the resulting high resolution stack after data selection and the inclusion of secondary tie-points. In order to better appreciate the quality of this record, Figure 7 shows enlargements of the stack for chrons 29n, 30n, 31n, 31r, 32n.2n, 33n and 33r together with the profiles used for the computation. The correlation among individual profiles and with the resulting stack is generally good.

Due to short-term spreading rate fluctuations, tiny wiggles may be slightly shifted from one profile to another resulting in smoother stacks, with wider anomalies and smaller amplitudes than the original profiles (see examples on Figure 7). Although not critical for the purpose of the present study, these effects should be kept in mind for the interpretation of the resulting stacks.

Following Cande and Kent [7,6,20], we model the identified tiny wiggles in terms of cryptochrons, i.e. polarity intervals shorter than 30 kyr. This choice is guided by three considerations. First, it makes comparisons between our results and the earlier results of Cande and Kent [7,6,20] most straightforward. Second, this representation is anyway a convenient zero-order equivalent representation of the observed geomagnetic variation signal. Third, as we shall see, it provides a simple mean to address the issue of the origin of tiny wiggles. We construct the cryptochron time scale by selecting consistent micro-anomalies that are observed both on the global stack and on regional stacks from at least two different areas. By doing so, eight uncertain tiny wiggles (marked as "possible" on Table 2) are no longer considered. The naming scheme of Cande and Kent [7,6] is hereafter adopted for the remaining cryptochrons. The center of the cryptochrons is estimated by localizing the minimum (maximum) of negative (positive) micro-anomaly in normal (reverse) polarity chrons as observed in the high resolution stack (red dots on Figure 6). We first set the duration of each cryptochron to 10 kyr and then adjust it so that the amplitude of observed and modeled micro-anomalies (normalized to the amplitude of the nearby reversal anomaly) is similar. The results are shown in Figure 6 and the ages of the cryptochrons are reported in Table 3 (see Electronic Supplement).

7 Discussion

Our study allows one to detect a large number of tiny wiggles which are either due to short polarity intervals or to large paleointensity fluctuations, the latter being possibly related to excursions generally associated with a large directional variation. For marine magnetic anomaly profiles, the Earth filter bandpass depends on the water depth and on the spreading rate [18]. Power spectra of individual sea-surface profiles used in this study show that the smallest wavelength above the noise level (for which

the spectrum is flat) is ~ 5 km which is about the water depth. For a spreading rate of 60 km/Myr, a wavelength of 5 km would correspond to a timescale of 80 kyr. This means that sharp geomagnetic variations such as polarity intervals or excursions occurring on timescales shorter than 80 kyr (but with some possible spectral content at timescales of 80 kyr and above) could produce anomalies with similar wavelengths as genuine intensity fluctuations on the 80 kyr timescale. Sea-surface magnetic anomaly profiles cannot distinguish between those two types of signal which, in addition, are likely smoothed and biased towards longer timescales by the stacking procedure (see above). As a result, the duration of individual geomagnetic events cannot be unambiguously determined. Total field marine magnetic profiles do not permit to discriminate between long-term paleointensity fluctuations and excursions which can be as short as 5-10 kyr [10].

Useful insight on the origin of tiny wiggles can however be gained from the few available high-resolution magnetostratigraphic paleointensity studies covering the past few Myr (see for instance, [25] for the Brunhes period; [26] for the Matuyama period; [27] for the Matuyama and late Gauss periods; [9] for the past 2 Myr; [8] for the past 4 Myr; [28] for chrons 5n; [29] for chrons 6Bn to 13n; [30] for chrons 12r to 13r). These studies have shown that the magnetic polarity time scale mainly determined from marine magnetic anomalies is almost complete and that only a few tiny wiggles detected so far can be ascribed to additional short polarity intervals (e.g. [31–33]). Most tiny wiggles thus appear to be due to geomagnetic intensity variations [6]. A similar conclusion is also suggested by recent deep-tow magnetic measurements which revealed a detailed pattern of micro-anomalies that correlates very well with paleointensity fluctuations inferred from magnetostratigraphic studies ([34], for the Brunhes period; [35,36] for the Brunhes and Matuyama periods; [37,28] for chron 5n.2n).

Our modeling of the tiny wiggles in terms of cryptochrons provides even more evidence and suggests that those conclusions also hold over the 83-41 Ma time period. Indeed, the duration of the cryptochrons we found varies from 2 kyr to 26 kyr (Table 3, see Electronic Supplement), 82% of these values being lower than 10 kyr. Considering that a full magnetic reversal does not take place in less than about five thousand years, and that polarity intervals can hardly be shorter than some ten thousand years (e.g. [38]) this again shows that most tiny wiggles must reflect paleointensity

fluctuations.

To further investigate the nature of tiny wiggles, we next look into their distribution within chrons. We compute the relative position of each tiny wiggle within each chron, i.e. the time elapsed since the beginning of the chron normalized to the duration of the chron. This parameter x varies between 0 (beginning of the chron) and 1 (end of the chron). The cumulative distribution function of this variable x is a straight line between $x = 0.1$ and 0.9 (Figure 8a). No tiny wiggle is found for values of x lower than about 0.1 and greater than about 0.9, i.e. within typically 10 km of a nearby reversal. This, we suggest, reflects the fact that the "secondary" signal of tiny wiggles is obscured by the main signal produced by reversals. Indeed, no tiny wiggle is detected for the shortest chrons and most identified tiny wiggles are indeed found in long chrons. Also, this could explain why few tiny wiggles have been detected so far within the past 30 Myr, a period characterized by a reversal frequency higher than that of the time interval investigated in the present study (e.g., [39]). As a matter of fact, computing the relative position x' of the tiny wiggle within each chron after excluding a "blind" zone of 10 km at both ends of the chron provides a simple picture. The resulting cumulative distribution function of x' then appears to be a straight line with a slope equal to 1 (Figure 8b), and suggests that the distribution of tiny wiggles is homogenous within chrons, except perhaps within the vicinity of reversals where no information is available.

This prompts us to assess the tiny wiggle frequency within each chron by simply taking the inverse of the average duration between successive tiny wiggles. As can be seen (Figure 9), this tiny wiggle frequency appears to be correlated with the mean spreading rate of the high resolution stack with a correlation coefficient of 0.87. This correlation is particularly clear for chrons 20r-24r and chron 29n, although some exceptions (for instance chrons 27r-28n) are also observed. This correlation shows up even after selecting areas characterized by the highest spreading rate for each chron and again underlines the strong influence of spreading rate on the detection of tiny wiggles. To directly check that this is indeed the case and to take into account the "blinding" effect discussed above, we next build a fictitious timescale by excluding time intervals bounded by two tiny wiggles and containing a reversal. For each event of this modified timescale, we plot the distance to the origin (the first

tiny wiggle) against the order of occurrence (Figure 10). As can be seen, all points fall on a straight line with a slope yielding a constant mean distance between tiny wiggles of ~ 16 km. Clearly, the possibility of detecting a tiny wiggle is more related to the amount of sea-floor available to record this geomagnetic signal than to the time elapsed. This behaviour can indeed be expected if tiny wiggles are mainly due to long-term paleointensity fluctuations. Geomagnetic secular variation includes a very large temporal spectrum which is fairly flat in the frequency range of interest here, with periods above ~ 50 kyr [40]. If tiny wiggles are a filtered record of this secular variation, increasing the spreading rates, simply amounts to increase the resolution of the magnetic record which will systematically increase the number of detected tiny wiggles per time units, but not the amount of tiny wiggles per units of seafloor. This is what we found with a spatial tiny wiggle frequency (one per 16 km) logically close to the resolution of the marine magnetic anomaly profiles (5 km).

Assuming from now on that tiny wiggles are indeed mainly due to paleointensity variations, it is next interesting to note that their uniform distribution within chrons as shown in Figure 8 would indicate that paleointensity variations are neither inhibited after, nor enhanced before, reversals beyond the "blind" period of about 10 km already identified (i.e. 250-80 kyr for spreading rates of 40-120 km/Myr). This behavior contrast with the long-term "memory" of the dipole field considered by Cande [41] to account for the anomalous skewness of marine magnetic anomalies, and by Valet and Meynadier [8] to account for the "sawtooth pattern" observed in the paleointensity fluctuations over the past 4 Myr. But it is not in contradiction with the recent update by Valet et al. [9], which now argues in favour of a slow decrease in paleointensity only during a period of about 60-80 kyr before reversals.

Finally our results would suggest that the secular variation remains rather uniform throughout the studied period. Although this conclusion only applies to the longer wavelengths of the secular variation that are attainable through the analysis of sea-surface magnetic anomalies, such a uniform behavior of the secular variation would strongly contrast with the marked variation of the reversal rate observed during the investigated period, increasing from zero during the Cretaceous Normal Superchron (118-83 Ma), to a reversal rate of about $2-3 \text{ Myr}^{-1}$ at ~ 40 Ma. Further analysis of high

resolution records such as deep-tow magnetic profiles should bring new constraints on this particular point.

Beyond their interest for geomagnetic studies, tiny wiggles are also useful as fine scale markers of seafloor spreading. Our new geomagnetic timescale over 42 Myr (Table 3, see Electronic Supplement) may therefore help to better identify major anomalies, increase the resolution of seafloor dating, and improve reconstructions of the plate tectonic history of oceanic basins (e.g. [42]).

Acknowledgments

We thank Philippe Patriat for providing us with the French data in the Indian Ocean. We are grateful to Clément Narteau and Jean-Louis Le Mouél for their help and comments. We also thank an anonymous reviewer for his constructive comments. This is IPGP contribution no. 2146.

Appendix A. Supplementary data

Supplementary data associated with this article can be found, in the online version, at [doi:10.1016/j.epsl.2006.06.051](https://doi.org/10.1016/j.epsl.2006.06.051).

References

- [1] R. J. Blakely, A. Cox, Evidence for short geomagnetic polarity intervals in the Early Cenozoic, *J. Geophys. Res.* 77 (1972) 7065–7072.
- [2] R. J. Blakely, Geomagnetic reversals and crustal spreading rates during the Miocene, *J. Geophys. Res.* 79 (1974) 2979–2985.
- [3] S. C. Cande, J. L. LaBrecque, Behavior of the Earth's paleomagnetic field from small scale marine magnetic anomalies, *Nature* 247 (1974) 26–28.

- [4] D. K. Rea, R. J. Blakely, Short-wavelength magnetic anomalies in a region of rapid seafloor spreading, *Nature* 255 (1975) 126–128.
- [5] D. S. Wilson, R. N. Hey, The Galapagos axial magnetic anomaly: Evidence for the Emperor event within the Brunhes and for a two-layer magnetic source, *Geophys. Res. Lett.* 8 (1981) 1051–1054.
- [6] S. C. Cande, D. V. Kent, Ultrahigh Resolution Marine Magnetic Anomaly Profiles: A Record of Continuous Paleointensity Variations?, *J. Geophys. Res.* 97 (1992) 15075–15083.
- [7] S. C. Cande, D. V. Kent, A New Geomagnetic Polarity Time Scale for the Late Cretaceous and Cenozoic, *J. Geophys. Res.* 97 (1992) 13917–13951.
- [8] J.-P. Valet, L. Meynadier, Geomagnetic field intensity and reversals during the past four million years, *Nature* 366 (1993) 234–238.
- [9] J.-P. Valet, L. Meynadier, Y. Guyodo, Geomagnetic dipole strength and reversal rate over the past two million years, *Nature* 435 (2005) 802–805.
- [10] C. G. Langereis, M. J. Dekkers, G. J. de Lange, M. Paterne, P. J. M. van Santvoort, Magnetostratigraphy and astronomical calibration of the last 1.1 Myr from an eastern Mediterranean piston core and dating of short events in the Brunhes, *Geophys. J. Int.* 129 (1997) 75–94.
- [11] S. C. Cande, J. L. LaBrecque, R. L. Larson, W. C. Pitman III, X. Golovchenko, W. F. Haxby, Magnetic lineations of the World's ocean basins (map), American Association of Petroleum Geologists, Tulsa, Oklahoma, 1989.
- [12] D. T. Sandwell, W. H. F. Smith, Marine gravity anomaly from Geosat and ERS-1 satellite altimetry, *J. Geophys. Res.* 102 (1997) 10039–10050.
- [13] P. Patriat, J. Achache, India-Eurasia collision chronology has implications for crustal shortening and driving mechanism of plates, *Nature* 311 (1984) 615–621.
- [14] P. Patriat, J. Segoufin, Reconstruction of the Central Indian Ocean, *Tectonophysics* 155 (1988) 211–234.
- [15] S. C. Cande, E. M. Herron, B. R. Hall, The early Cenozoic tectonic history of the southeast Pacific, *Earth Planet. Sci. Lett.* 57 (1982) 63–74.

- [16] D. McAdoo, S. Laxon, Antarctic Tectonics: Constraints From an ERS-1 Satellite Marine Gravity Field, *Science* 276 (1997) 556–560.
- [17] C. E. Barton, R. T. Baldwin, D. R. Barraclough, S. Bushati, M. Chiappini, Y. Cohen, R. Coleman, G. Hulot, P. Kotze, V. P. Golovkov, A. Jackson, R. A. Langel, F. J. Lowes, D. J. McKnight, S. MacMillan, L. R. Newitt, N. W. Peddie, J. M. Quinn, T. J. Sabaka, International Geomagnetic Reference Field, 1995 revision Presented by IAGA Division V, Working Group 8, *Phys. Earth Planet. Int.* 97 (1996) 23–26.
- [18] H. Schouten, K. McCamy, Filtering marine magnetic anomalies, *J. Geophys. Res.* 77 (1972) 7089–7099.
- [19] M. Talwani, J. R. Heirtzler, Computation of magnetic anomalies caused by two dimensional structures of arbitrary shape, in: G. Parks (Ed.), *Computers in the mineral industries*, Vol. 9, Stanford Univ. Publ., Stanford, California, 1964, pp. 464–480.
- [20] S. C. Cande, D. V. Kent, Revised calibration of the geomagnetic polarity timescale for the late Cretaceous and Cenozoic, *J. Geophys. Res.* 100 (1995) 6093–6095.
- [21] S. C. Cande, D. V. Kent, Constraints Imposed by the Shape of Marine Magnetic Anomalies on the Magnetic Source, *J. Geophys. Res.* 81 (1976) 4157–4162.
- [22] J. Dyment, S. C. Cande, J. Arkani-Hamed, Skewness of marine magnetic anomalies created between 85 and 40 Ma in the Indian Ocean, *J. Geophys. Res.* 99 (1994) 24121–24134.
- [23] J. Dyment, J. Arkani-Hamed, Spreading rate dependent magnetization of the oceanic lithosphere inferred from the anomalous skewness of marine magnetic anomalies, *Geophys. J. Int.* 121 (1995) 789–804.
- [24] B. Parsons, J. G. Sclater, An analysis of the variation of ocean floor bathymetry and heat flow with age, *J. Geophys. Res.* 82 (1977) 802–827.
- [25] Y. Guyodo, J.-P. Valet, Global changes in intensity of the Earth's magnetic field during the past 800 kyr, *Nature* 399 (1999) 249–252.
- [26] Y. S. Kok, L. Tauxe, A relative geomagnetic paleointensity stack from Ontong-Java Plateau sediments for the Matuyama, *J. Geophys. Res.* 104 (1999) 25401–25414.
- [27] T. Yamazaki, H. H. Oda, A geomagnetic paleointensity stack between 0.8 and 3.0 Ma from equatorial Pacific sediment cores, *Geochem., Geophys., Geosyst.* 6 (2005) Q11H20, doi:10.1029/2005GC001001.

- [28] J. Bowles, L. Tauxe, J. Gee, D. McMillan, S. Cande, Source of tiny wiggles in Chron C5: A comparison of sedimentary relative intensity and marine magnetic anomalies, *Geochem., Geophys., Geosyst.* 4(6) (2003) 1049, doi:10.1029/2002GC000489.
- [29] L. Tauxe, P. Hartl, 11 million years of Oligocene geomagnetic field behaviour, *Geophys. J. Int.* 128 (1997) 217–229.
- [30] L. Lanci, W. Lowrie, Magnetostratigraphic evidence that "tiny wiggles" in the oceanic magnetic anomaly record represent geomagnetic paleointensity variations, *Earth Planet. Sci. Lett.* 148 (1997) 581–592.
- [31] J. M. Parés, L. Lanci, A complete Middle Eocene-Early Miocene magnetic polarity stratigraphy in Equatorial Pacific sediments (ODP Site 1220), in: J. E. T. Channell, D. V. Kent, W. Lowrie, J. Meert (Eds.), *Timescales of the Paleomagnetic Field*, Vol. 145, AGU Geophysical Monograph, 2004, pp. 131–140.
- [32] W. Krijgsman, D. V. Kent, Non-uniform occurrence of short-term polarity fluctuations in the geomagnetic field? New results from Middle to Late Miocene sediments of the North Atlantic (DSDP Site 608), in: J. E. T. Channell, D. V. Kent, W. Lowrie, J. Meert (Eds.), *Timescales of the Paleomagnetic Field*, Vol. 145, AGU Geophysical Monograph, 2004, pp. 161–174.
- [33] G. Acton, Y. Guyodo, S. Brachfeld, The nature of a cryptochron from a paleomagnetic study of chron C4r.2r recorded in sediments off the Antarctic Peninsula, *Phys. Earth Planet. Int.* 156 (2006) 213–222.
- [34] J. S. Gee, S. C. Cande, J. A. Hildebrand, K. Donnelly, R. L. Parker, Geomagnetic intensity variations over the past 780 kyr obtained from near-seafloor magnetic anomalies, *Nature* 408 (2000) 827–832.
- [35] G. Pouliquen, Y. Gallet, J. Dyment, P. Patriat, C. Tamura, Correction to "A geomagnetic record over the last 3.5 million years from deep-tow magnetic anomaly profiles across the Central Indian Ridge", *J. Geophys. Res.* 106 (2001) 30549.
- [36] G. Pouliquen, Y. Gallet, J. Dyment, P. Patriat, C. Tamura, A geomagnetic record over the last 3.5 million years from deep-tow magnetic anomaly profiles across the Central Indian Ridge, *J. Geophys. Res.* 106 (2001) 10941–10960.
- [37] N. E. Bowers, S. C. Cande, J. S. Gee, J. A. Hildebrand, R. L. Parker, Fluctuations of the paleomagnetic

field during chron C5 as recorded in near-bottom marine magnetic anomaly data, *J. Geophys. Res.* 106 (2001) 26379–26396.

[38] B. M. Clement, Dependence of the duration of geomagnetic polarity reversals on site latitude, *Nature* 428 (2004) 637–640.

[39] Y. Gallet, V. Courtillot, Geomagnetic reversal behaviour since 100 Ma, *Phys. Earth Planet. Int.* 92 (1995) 235–244.

[40] C. Constable, C. Johnson, A paleomagnetic power spectrum, *Phys. Earth Planet. Int.* 153 (2005) 61–73.

[41] S. C. Cande, Anomalous behavior of the paleomagnetic field inferred from the skewness of anomalies 33 and 34, *Earth Planet. Sci. Lett.* 40 (1978) 275–286.

[42] J. Dyment, Evolution of the Carlsberg Ridge between 60 and 45 Ma: Ridge propagation, spreading asymmetry, and the Deccan-Reunion hotspot, *J. Geophys. Res.* 103 (1998) 24067–24084.

List of Figures

- 1 Map of the World's oceanic magnetic lineations (in blue), after Cande et al. [11]. The areas selected in our study are in red and the selected profiles in black.
Areas in the Indian Ocean: 1. Central Indian Basin, east of the Indian Ocean Triple Junction trace; 2. Central Indian Basin, west of the Indian Ocean Triple Junction trace; 3. Crozet Basin; 4. Madagascar Basin; 5. Wharton Basin;
Areas in the North Pacific: 6. Aleutian Abyssal Plain, north of Chinook Trough; 7. Aleutian Abyssal Plain, north of Mendocino Fracture Zone (FZ); 8. Pacific Plate between Mendocino and Murray FZ; 9. Pacific Plate between Murray and Molokai FZ; 10. Pacific Plate between Molokai and Clarion FZ;
Areas in the South Pacific: 11. Pacific Plate south of FZ 8.5; 12. Pacific Plate north of FZ 8.5 and south of Heezen FZ; 13. Pacific Plate north of Heezen FZ; 14. Antarctic Plate south of Heezen FZ; 15. Antarctic Plate between Humbolt FZ and FZ V; 16. Antarctic Plate between FZ V and Heezen FZ. 26

- 2 Stacks computed in the different areas from the Indian (a), North Pacific (b) and South Pacific (c) oceans and global stacks calculated with all profiles available in the corresponding ocean. The stacks are drawn in red if they are computed with only one or two profiles. We report most tiny wiggles (blue ticks). The dashed lines indicate the correlations between stacks. For each ocean, the number of profiles available for each magnetic polarity interval in each ocean is also specified. 27

- 3 Mean (half) spreading rates computed in the different areas from the Indian (a), North Pacific (b) and South Pacific (c) oceans. The gray line indicate the mean spreading rate averaged for each ocean. 30

- 4 Application of the upward continuation method which allows one to compare stacks from different areas. For each chron, the stack computed for the area characterized by the fastest spreading rate (or eventually an area with enough profiles to be representative) is selected (second black curve from bottom), upward-continued (gray curves) and then compared to stacks from other areas (black curves) having various slower spreading rates. The global high resolution stack is also represented (black curve at the bottom). Micro-anomalies are shown by dots and correlations with the upward-continued stack are marked by dotted line. For chrons 25r, 26r and 33r, two panels are presented with upward-continued stacks from two different areas. 33
- 5 Stacks computed for chron 33n, that take into account secondary tie-points B and C (marked by gray vertical lines). The vertical scale has been adjusted so that the amplitude is the same for all areas. The number of profiles used in the computation and the mean half-spreading rate are specified for each area. 37
- 6 High resolution stack based on selected areas with the highest spreading rate. Tiny wiggles are marked by red dots. A model has been computed to the pole (i.e. assuming vertical magnetization and magnetic field vectors) using the geomagnetic polarity timescale of Cande and Kent [20] and incorporating the cryptochrons deduced from this study (Table 3, see Electronic Supplement). 38
- 7 Individual profiles used to compute the high resolution stack, for chrons 29n, 30n, 31n and 31r (a) and for chrons 32n.2n, 33n and 33r (b). A, B, C are secondary tie-points (see text). The name of cruises is specified according the scheme of NGDC database (<http://www.ngdc.noaa.gov/mgg/fliers/03mgg02.html>) and the French database for the Indian Ocean (http://barkeria.u-strasbg.fr/archivage/diffu_indien.html). The extension after the dash sign indicates the profile number when several profiles were obtained during the same cruise. Our area number is also given. 39

- 8 Cumulative distribution function (CDF) of the relative positions x and x' of tiny wiggles within the polarity events respectively before (a) and after the rejection of a “blind” zone of ~ 10 km at both ends of the chron (b). 41
- 9 Frequency of tiny-wiggles within each chron (in black) and mean spreading rate (in red) computed using the high resolution stack. Chrons having less than two tiny wiggles are not shown. The black bars are shorter than the chron durations because our frequency estimates were performed between the first and last tiny wiggles in order to exclude the “blind” period at both ends of chrons. 42
- 10 Distance as a function of the order of occurrence of each tiny wiggle in a fictitious timescale that excludes the time intervals bounded by two tiny wiggles and containing a reversal. The dots define a straight line yielding a constant mean distance of ~ 16 km between successive tiny wiggles. The name of the longer chrons are reported for reference. 43

List of Tables

- 1 Spreading directions and skewness corrections applied to profiles in the Indian (a), North Pacific (b) and South Pacific (c) oceans. 44
- 2 Description and comparison of the regional stacks for each chron, with the list of areas where the spreading rate allows a high (HR) or medium (MR) resolution record of the geomagnetic field fluctuations. We summarize the stack consistency with the other stacks and the number of identified tiny wiggles. 45
- 3 Cryptochrons found in our study from chron 19r to chron 33r. Names follow the convention of Cande and Kent [7,6]. 46

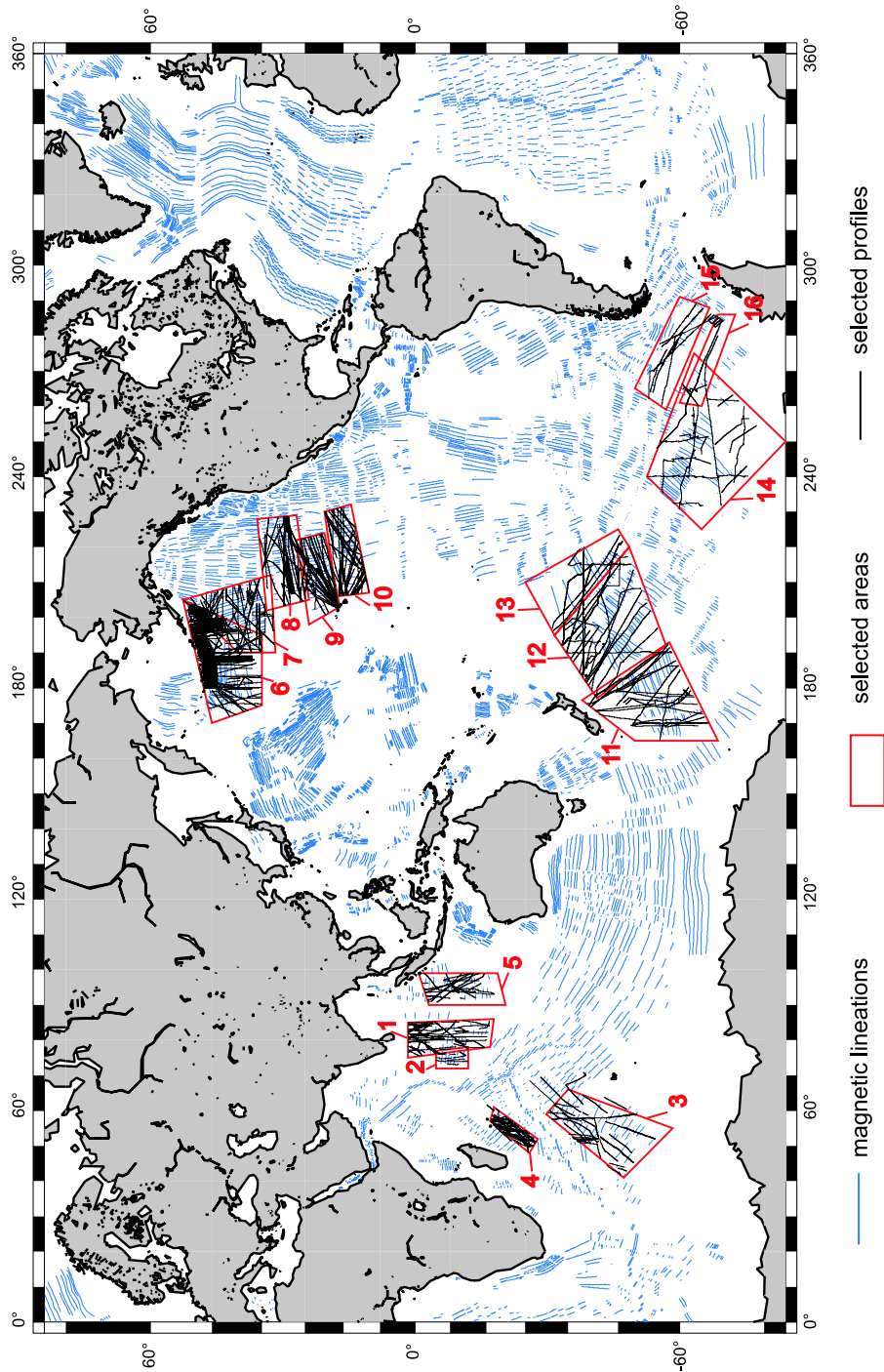


Fig. 1. Map of the World's oceanic magnetic lineations (in blue), after Cande et al. [11]. The areas selected in our study are in red and the selected profiles in black.

Areas in the Indian Ocean: 1. Central Indian Basin, east of the Indian Ocean Triple Junction trace; 2. Crozet Basin; 4. Madagascar Basin; 5. Wharton Basin; Areas in the North Pacific: 6. Aleutian Abyssal Plain, north of Chinook Trough; 7. Aleutian Abyssal Plain, north of Mendocino Fracture Zone (FZ); 8. Pacific Plate between Mendocino and Murray FZ; 9. Pacific Plate between Murray and Molokai FZ; 10. Pacific Plate between Molokai and Clarion FZ; Areas in the South Pacific: 11. Pacific Plate south of FZ 8.5; 12. Pacific Plate north of FZ 8.5 and south of Heezen FZ; 13. Pacific Plate north of Heezen FZ; 14. Antarctic Plate south of Heezen FZ; 15. Antarctic Plate between Humbolt FZ and FZ V; 16. Antarctic Plate between FZ V and Heezen FZ.

(a)

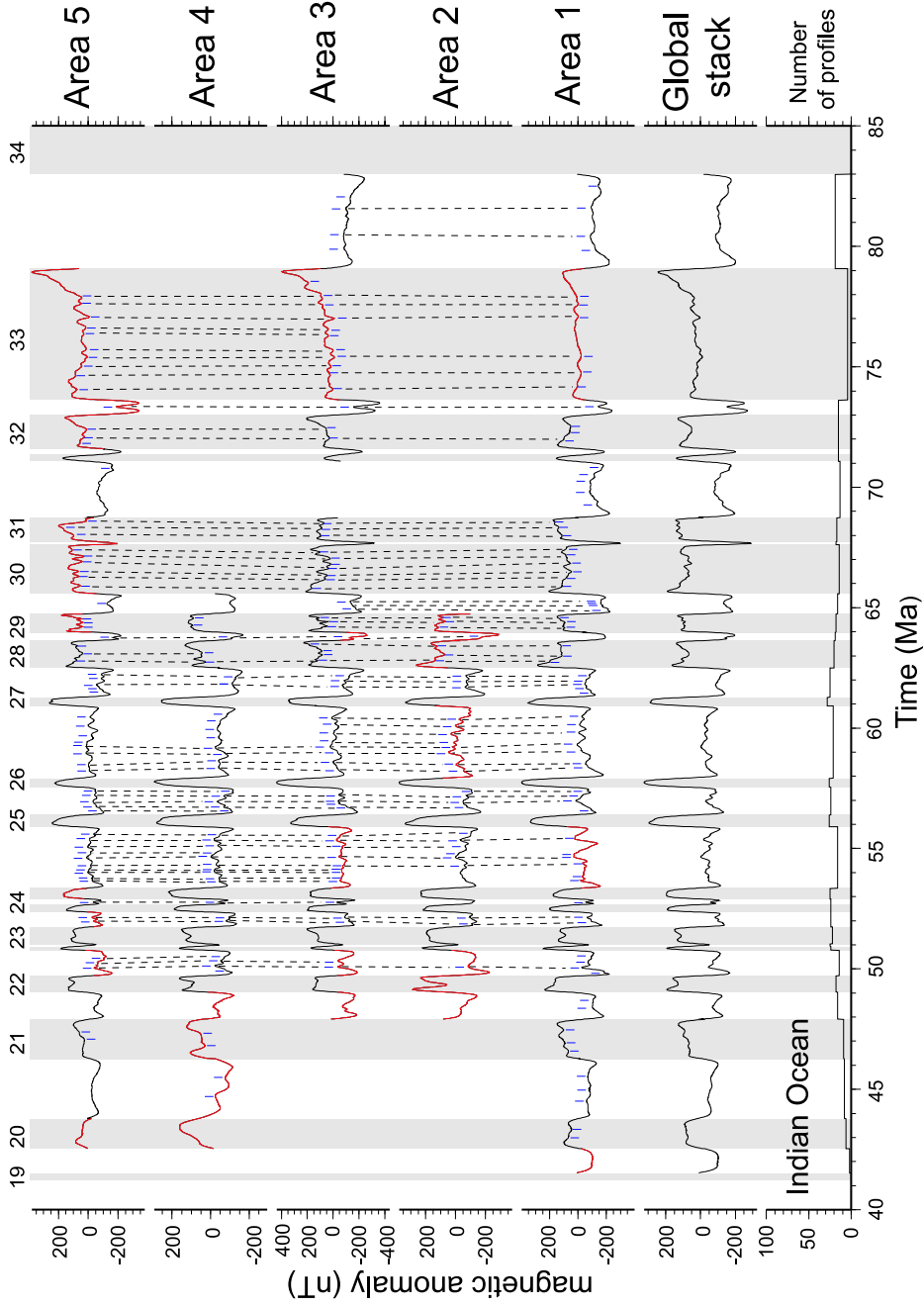
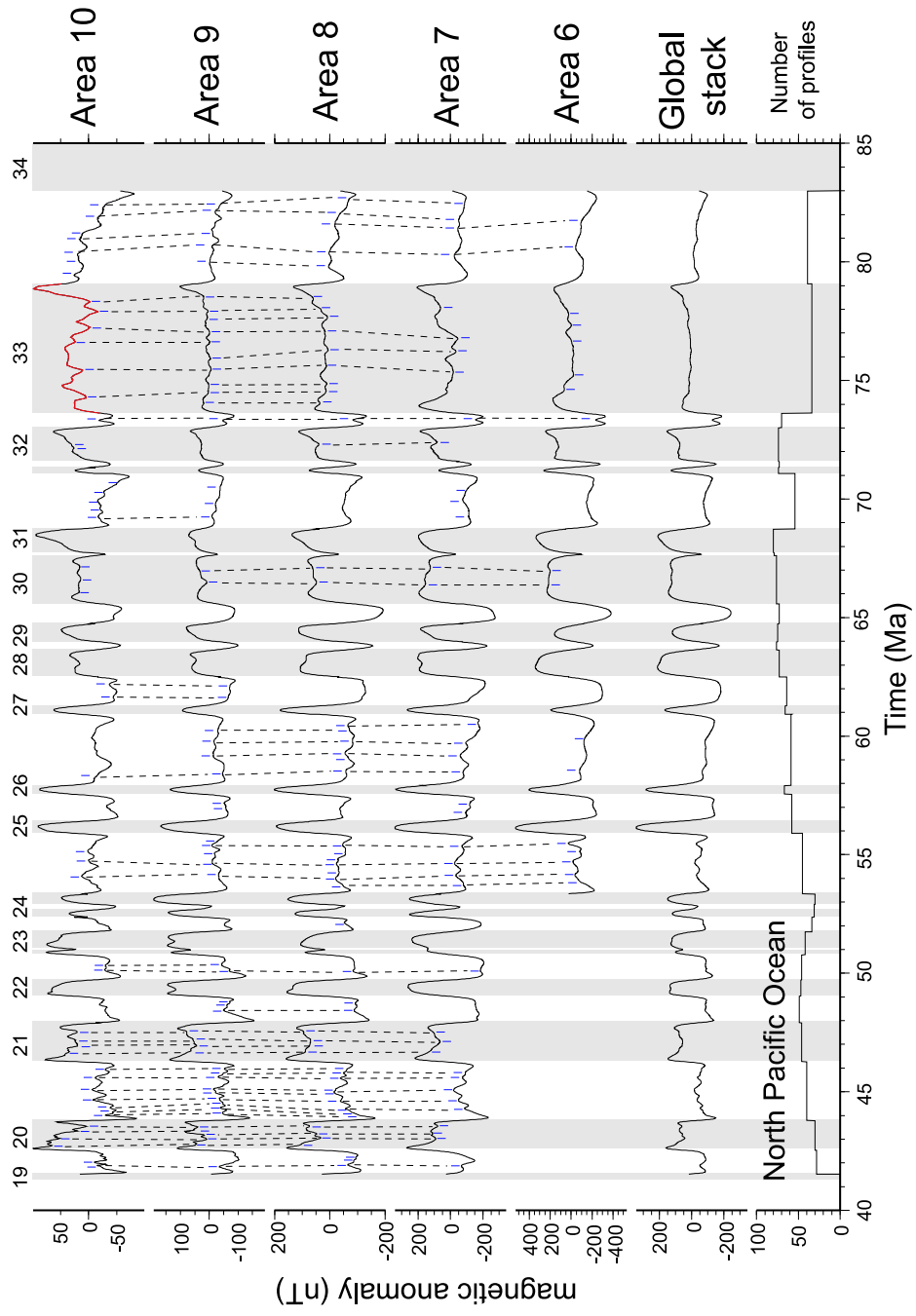
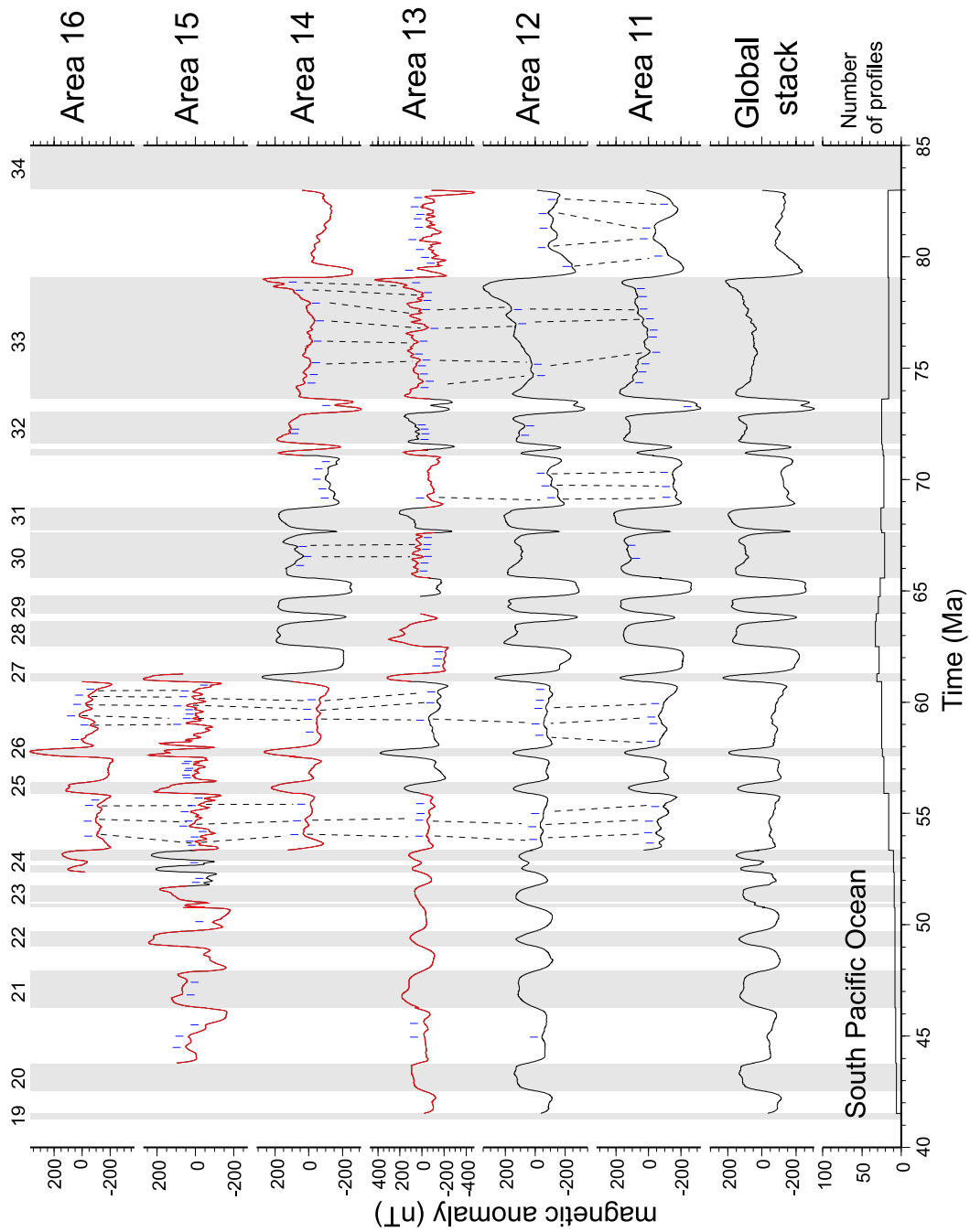


Fig. 2. Stacks computed in the different areas from the Indian (a), North Pacific (b) and South Pacific (c) oceans and global stacks calculated with all profiles available in the corresponding ocean. The stacks are drawn in red if they are computed with only one or two profiles. We report most tiny wiggles (blue ticks). The dashed lines indicate the correlations between stacks. For each ocean, the number of profiles available for each magnetic polarity interval in each ocean is also specified.

(b)



(c)



(a)

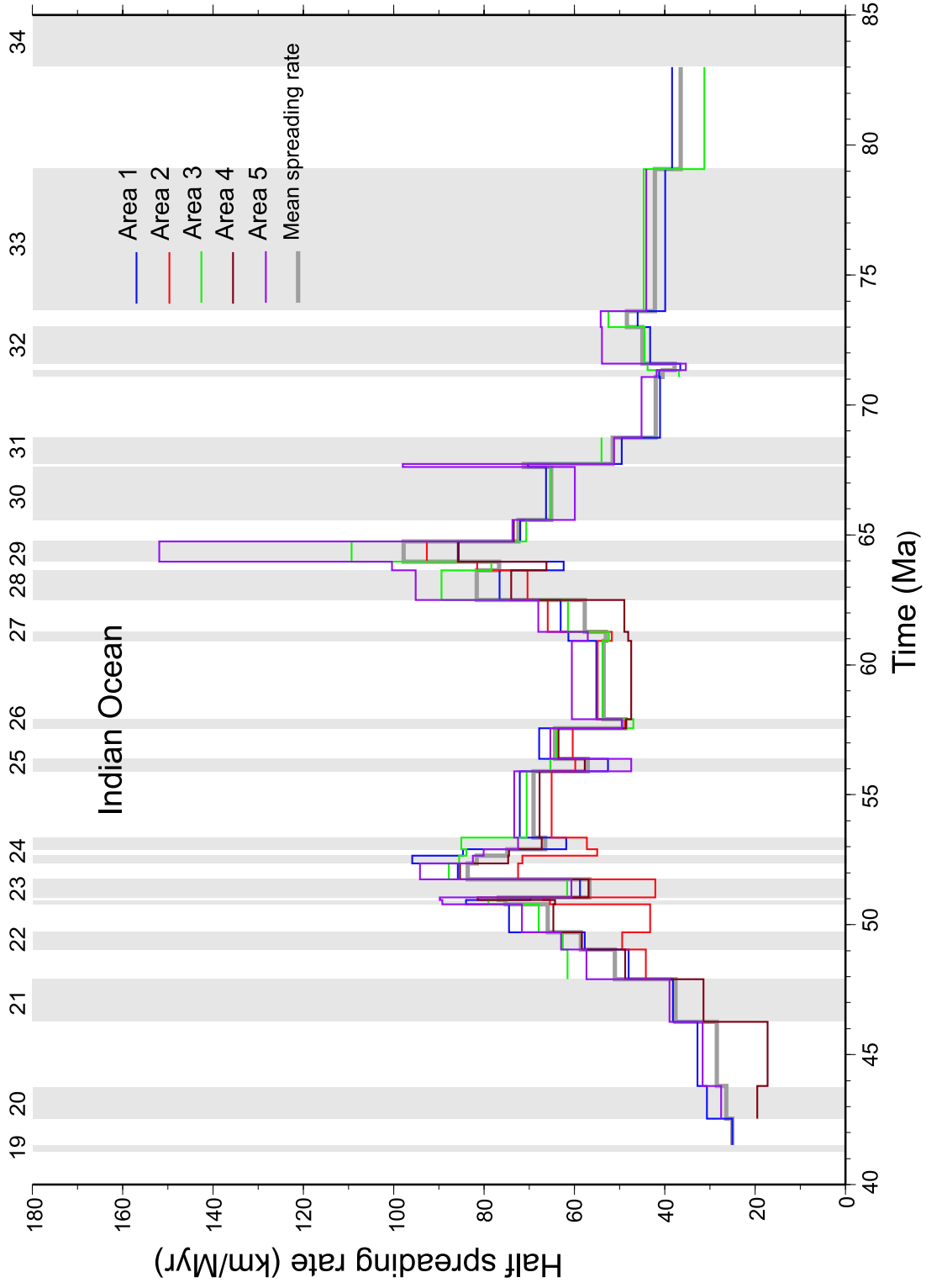
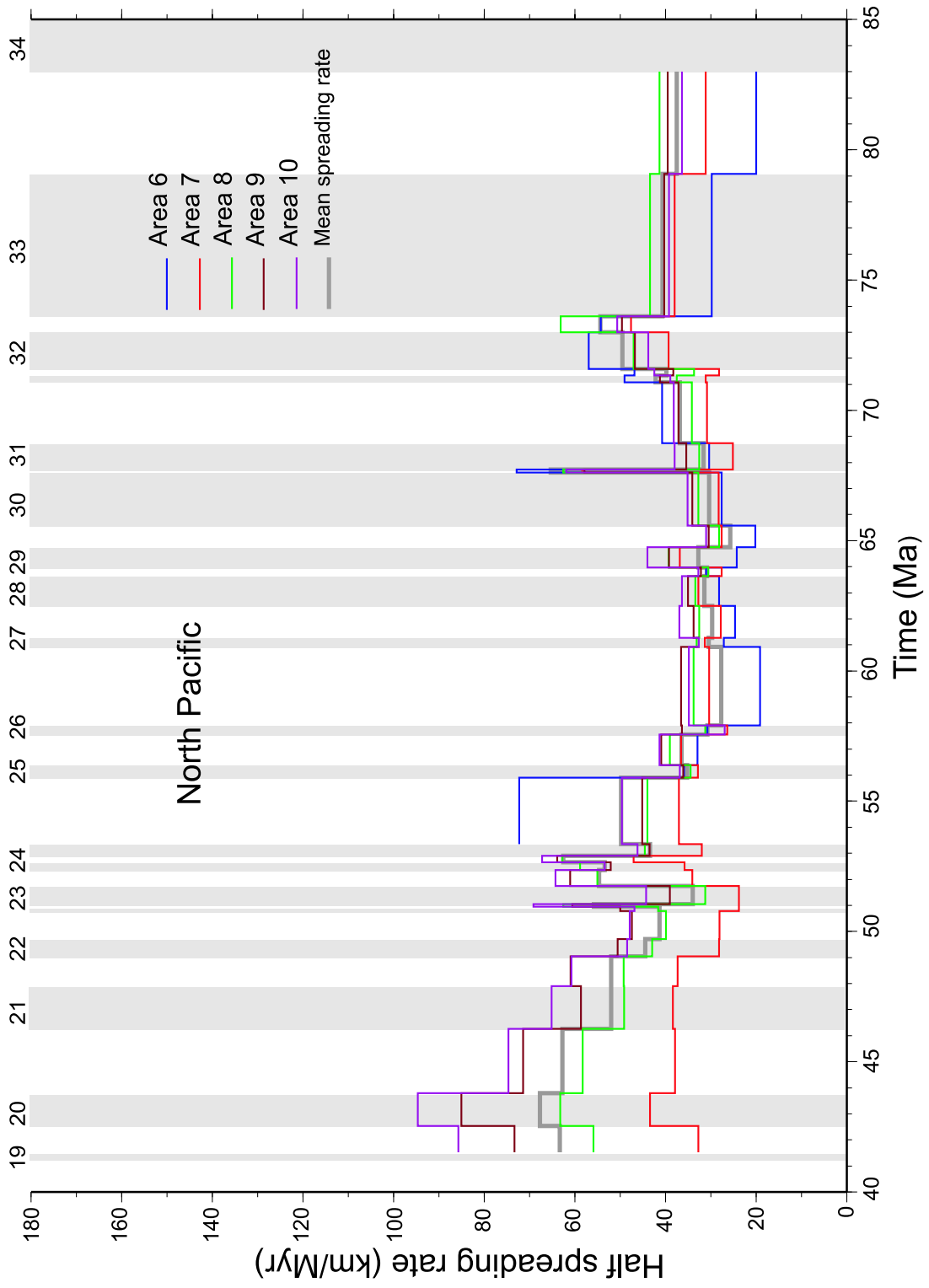
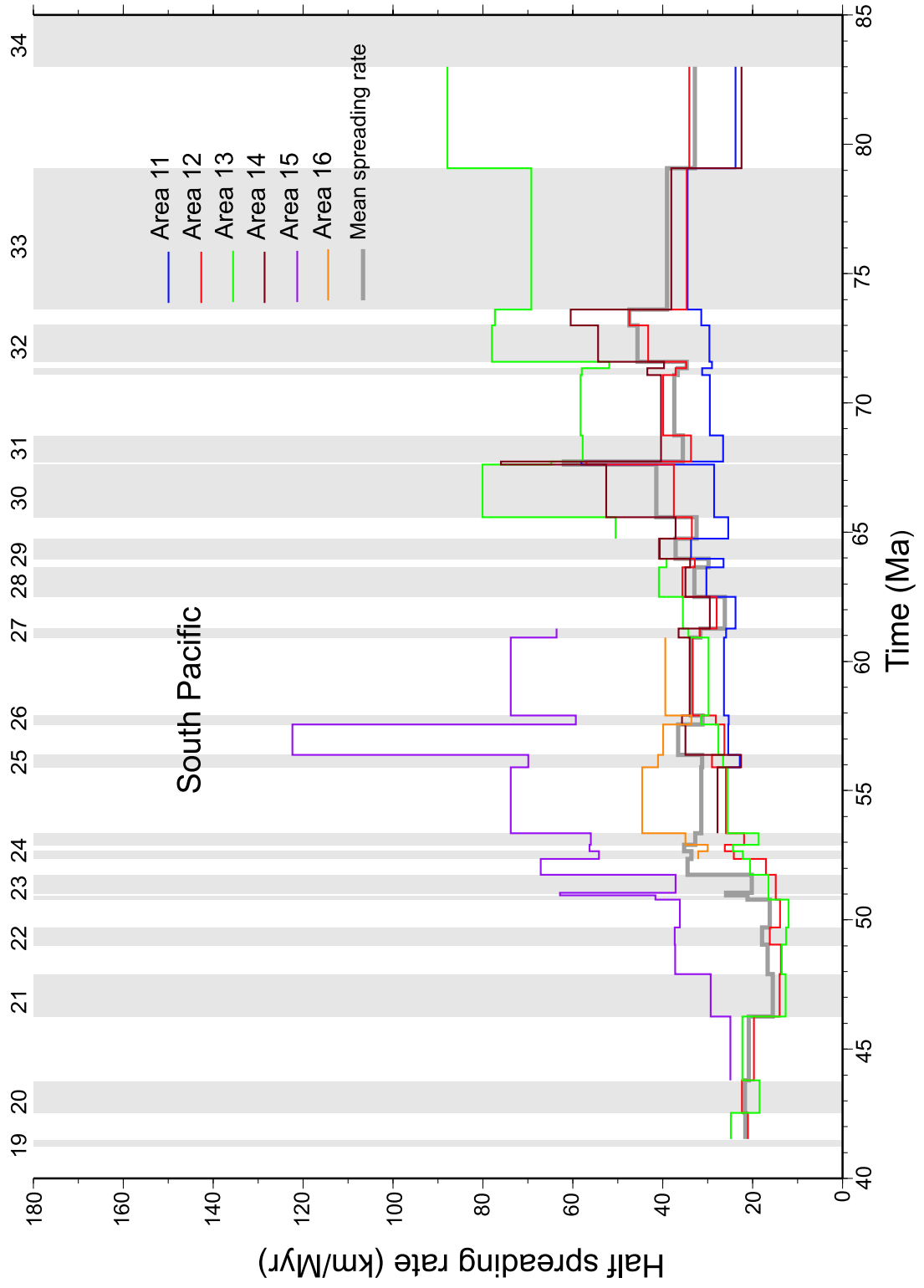


Fig. 3. Mean (half) spreading rates computed in the different areas from the Indian (a), North Pacific (b) and South Pacific (c) oceans. The gray line indicate the mean spreading rate averaged for each ocean.

(b)



(c)



(a)

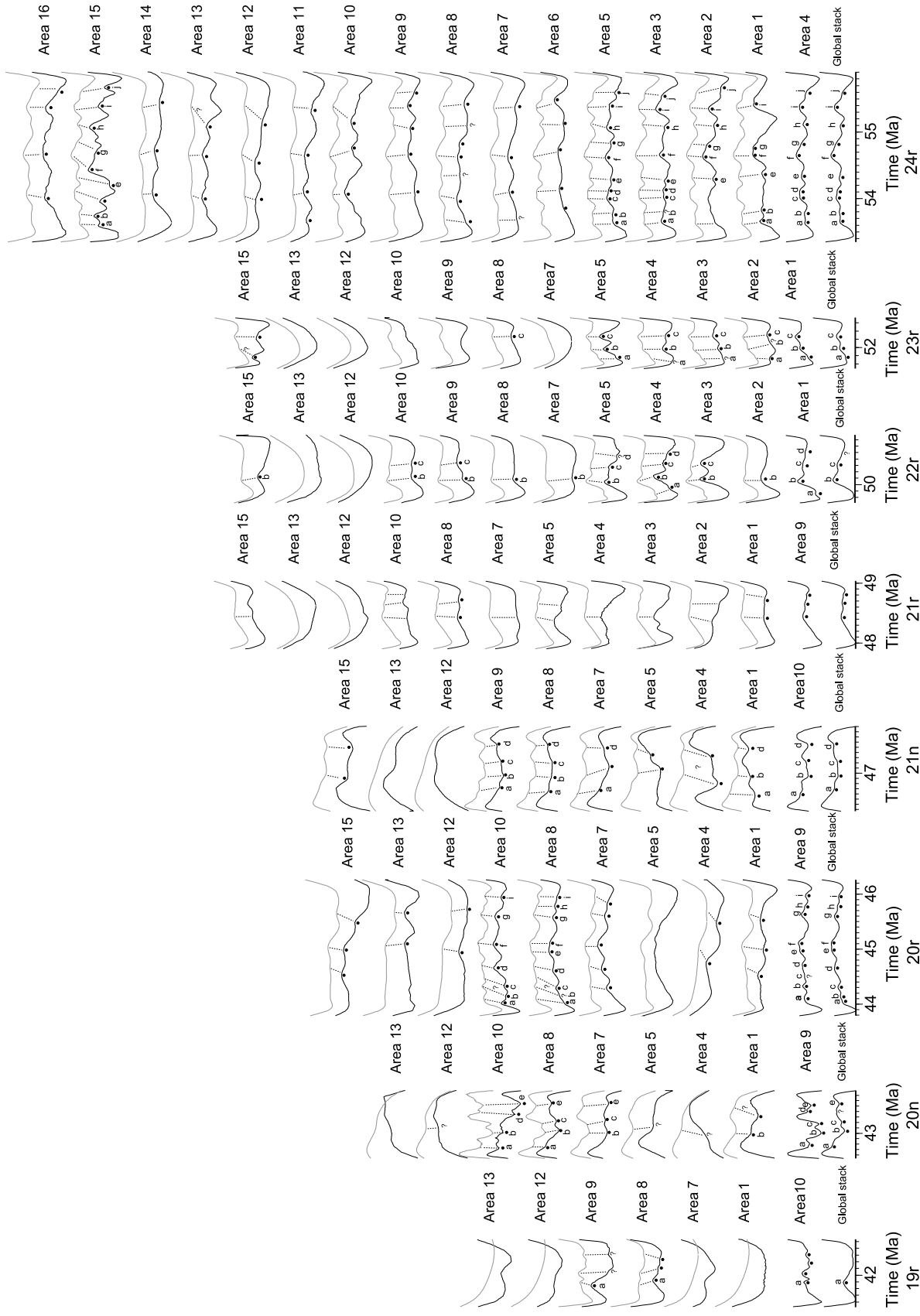
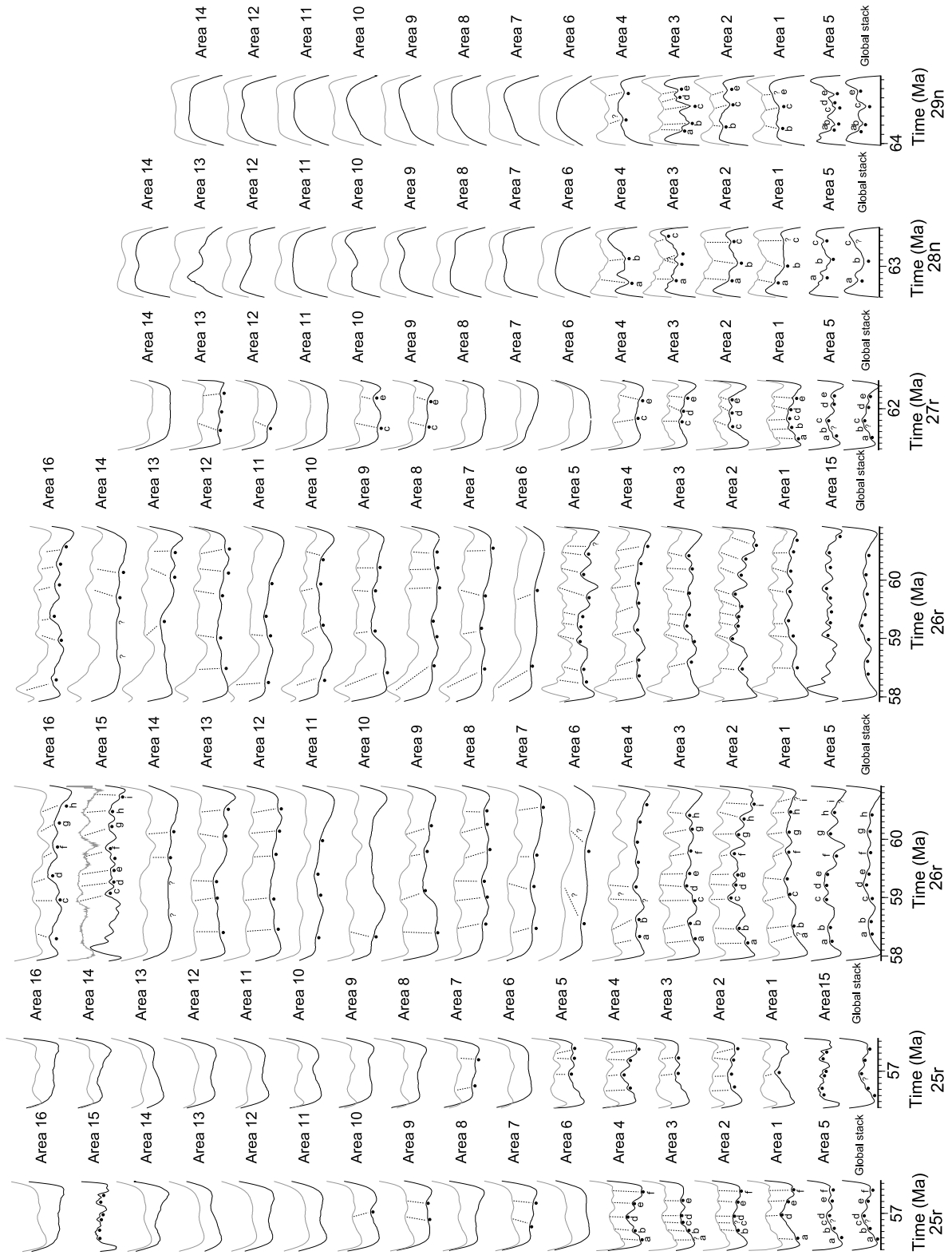
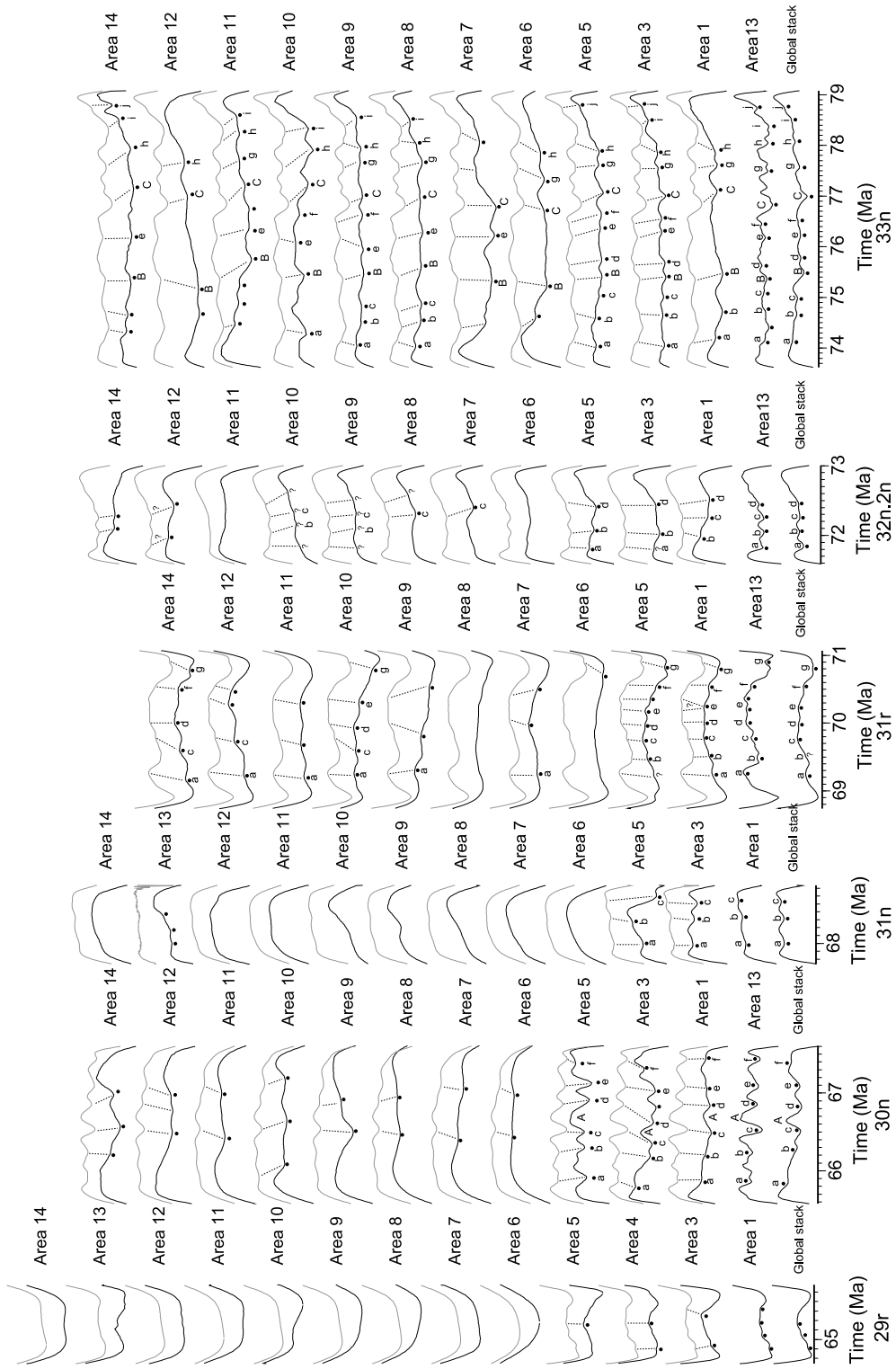


Fig. 4. Application of the upward continuation method which allows one to compare stacks from different areas. For each chron, the stack computed for the area characterized by the fastest spreading rate (or eventually an area with enough profiles to be representative) is selected (second black curve from bottom), upward-continued (gray curves) and then compared to stacks from other areas (black curves) having various slower spreading rates. The global high resolution stack is also represented (black curve at the bottom). Micro-anomalies are shown by dots and correlations with the upward-continued stack are marked by dotted line. For chrons 25r, 26r and 33r, two panels are presented with upward-continued stacks from two different areas.

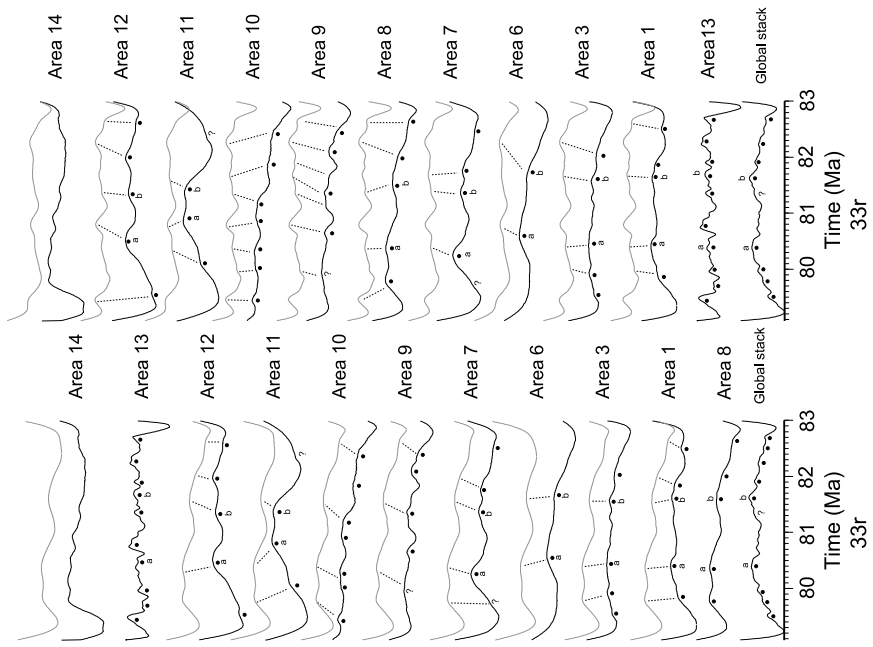
(b)



(c)



(d)



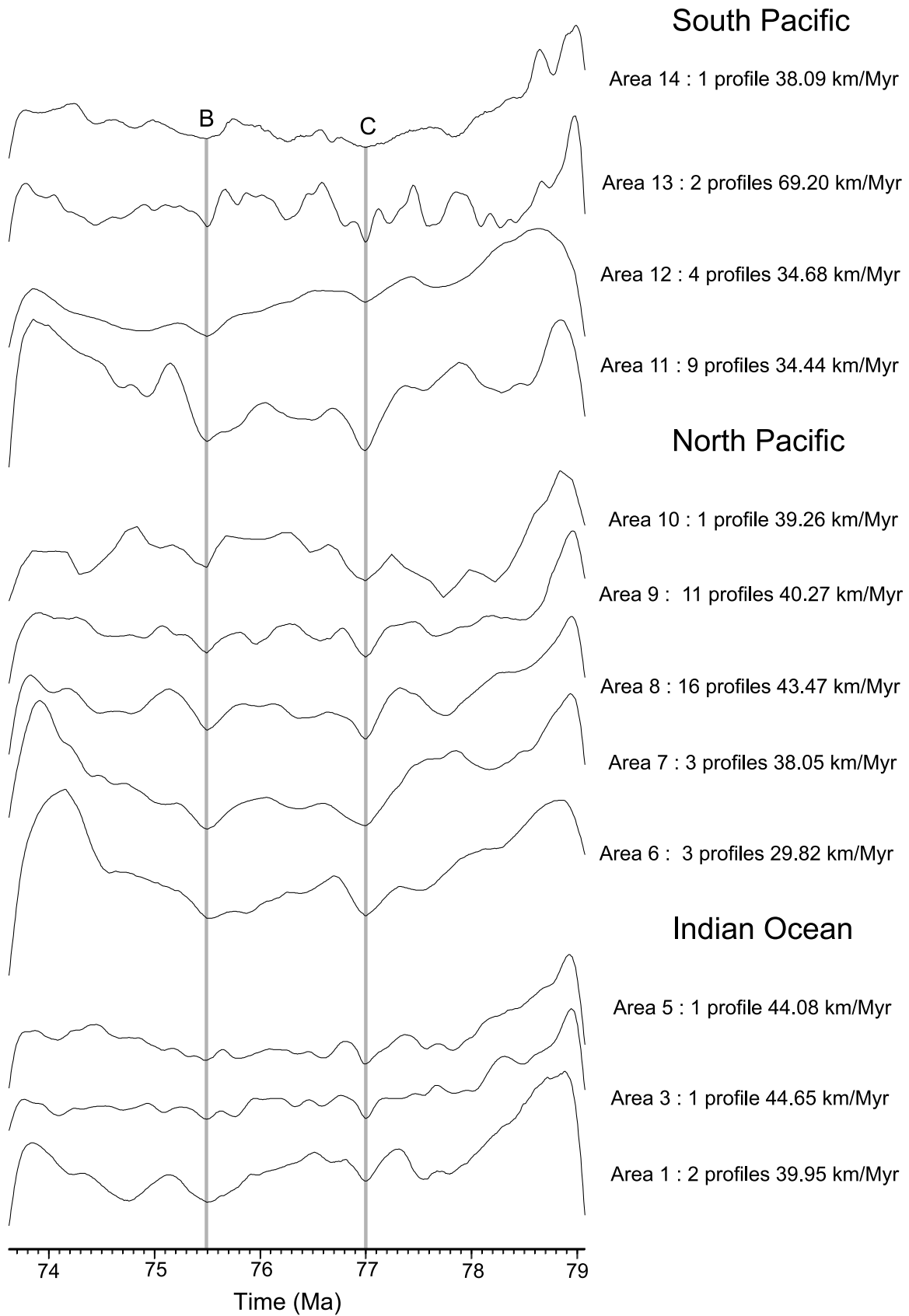


Fig. 5. Stacks computed for chron 33n, that take into account secondary tie-points B and C (marked by gray vertical lines). The vertical scale has been adjusted so that the amplitude is the same for all areas. The number of profiles used in the computation and the mean half-spreading rate are specified for each area.

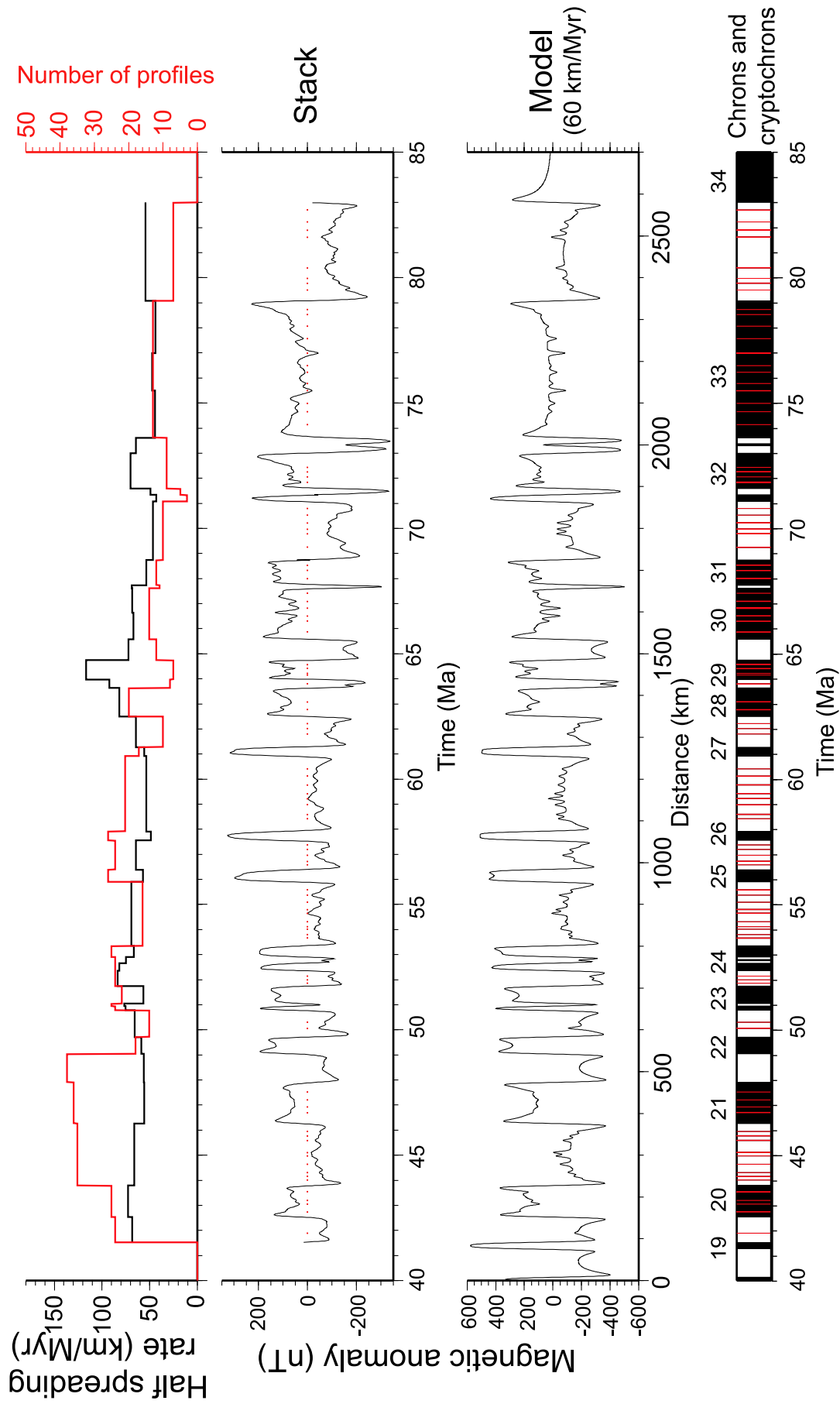


Fig. 6. High resolution stack based on selected areas with the highest spreading rate. Tiny wiggles are marked by red dots. A model has been computed to the pole (i.e. assuming vertical magnetization and magnetic field vectors) using the geomagnetic polarity timescale of Cande and Kent [20] and incorporating the cryptochrons deduced from this study (Table 3, see Electronic Supplement).

(a)

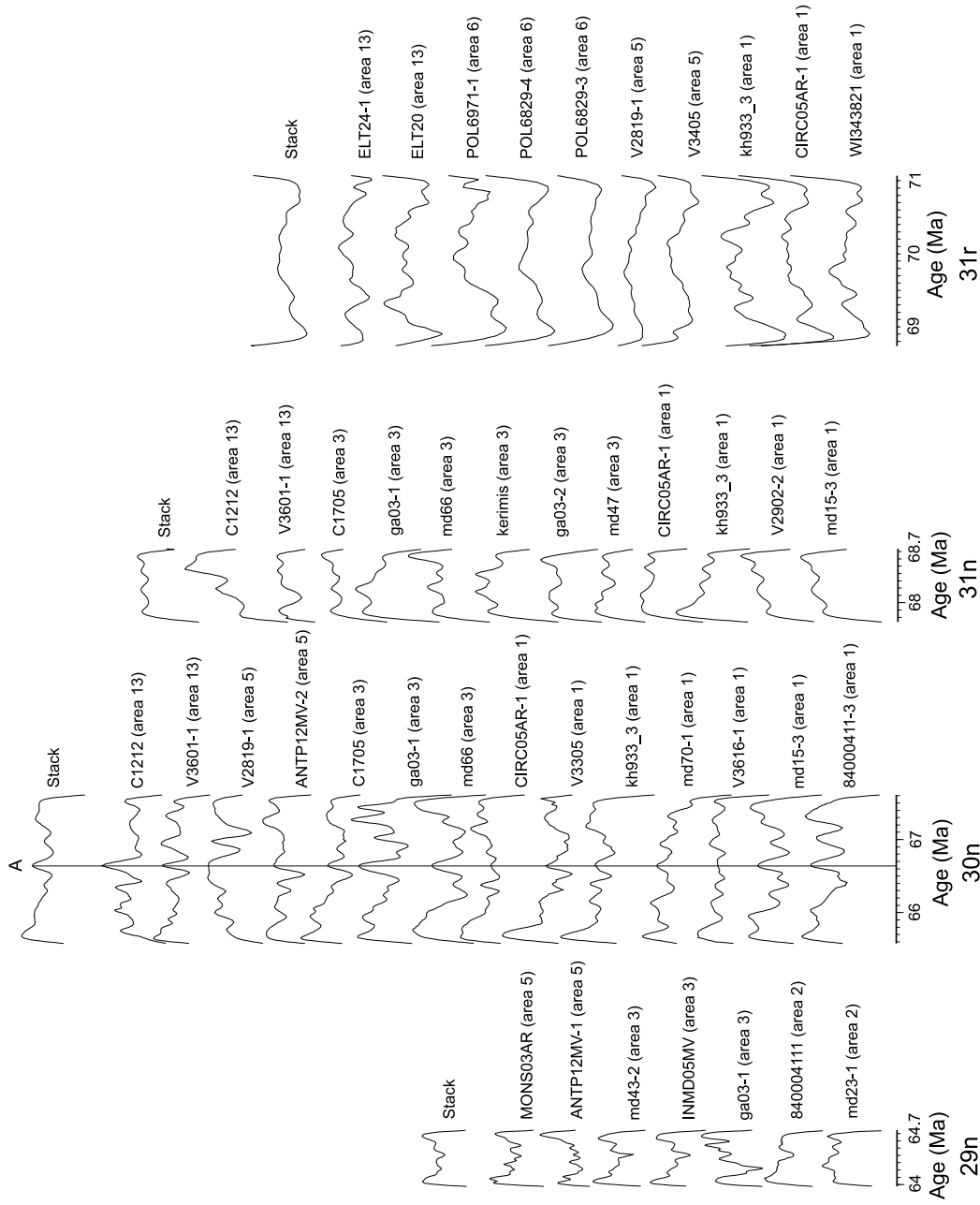
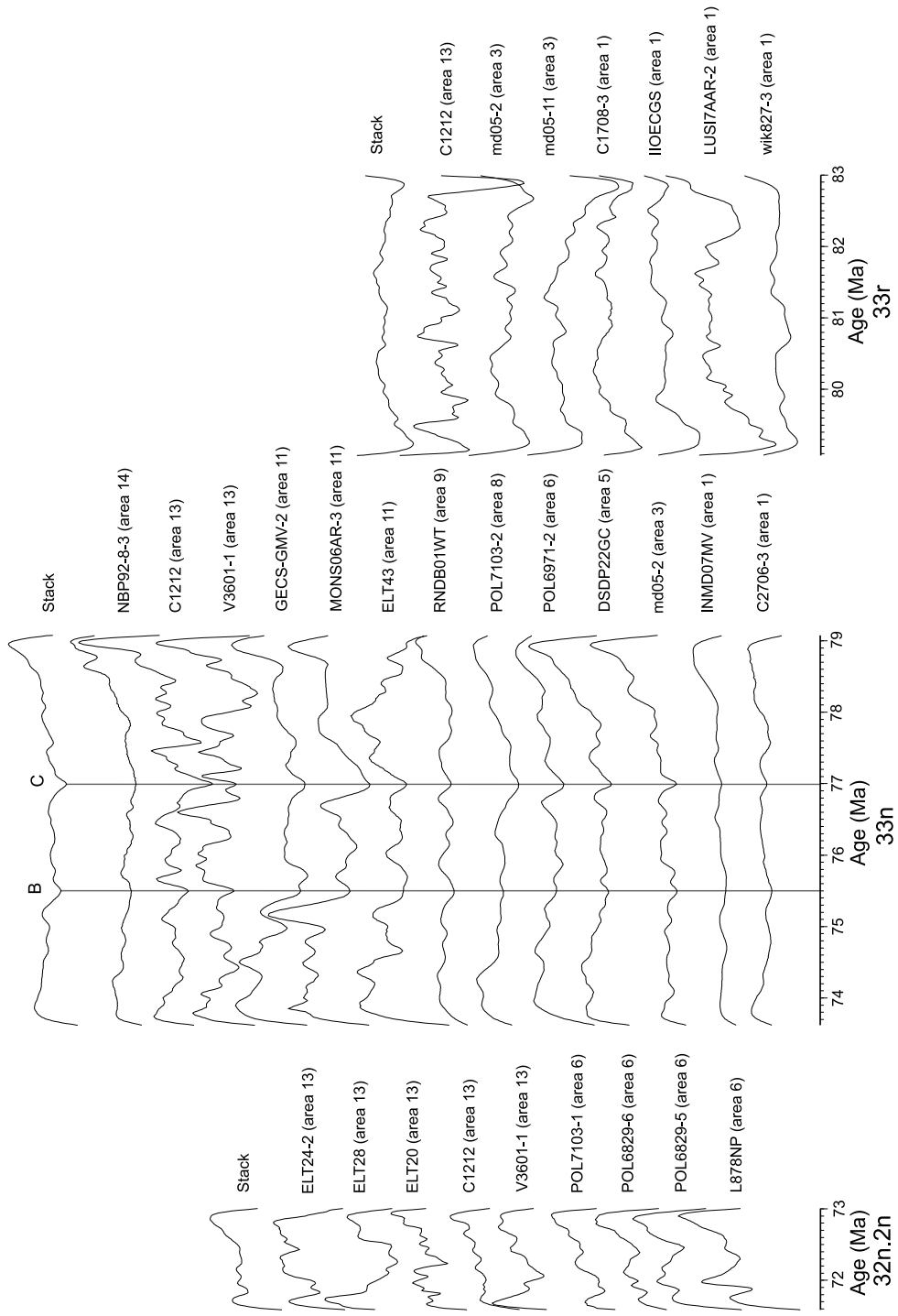
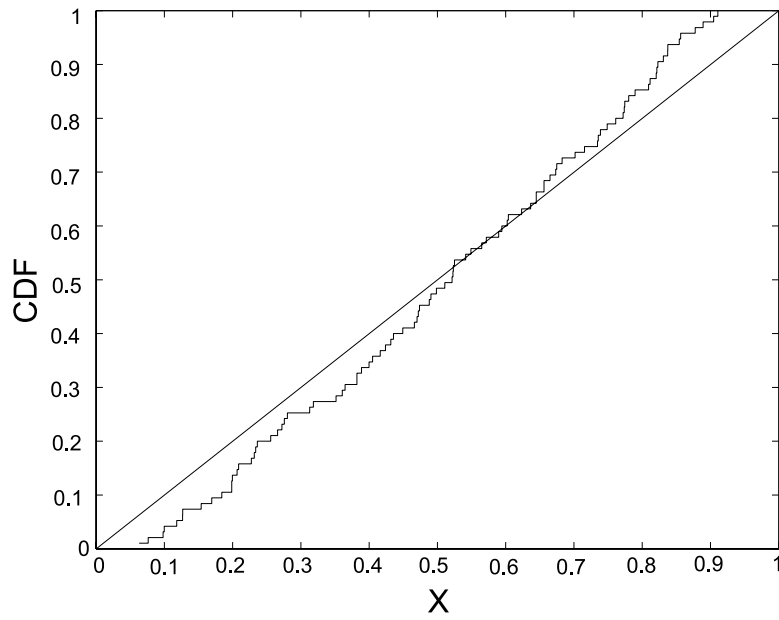


Fig. 7. Individual profiles used to compute the high resolution stack, for chrons 29n, 30n, 31n and 31r (a) and for chrons 32n, 2n, 33n and 33r (b). A, B, C are secondary tie-points (see text). The name of cruises is specified according the scheme of NGDC database (<http://www.ngdc.noaa.gov/mgg/fliers/03mgg02.html>) and the French database for the Indian Ocean (http://barberia.u-strasbg.fr/archivage/diffu_indien.html). The extension after the dash sign indicates the profile number when several profiles were obtained during the same cruise. Our area number is also given.

(b)



(a)



(b)

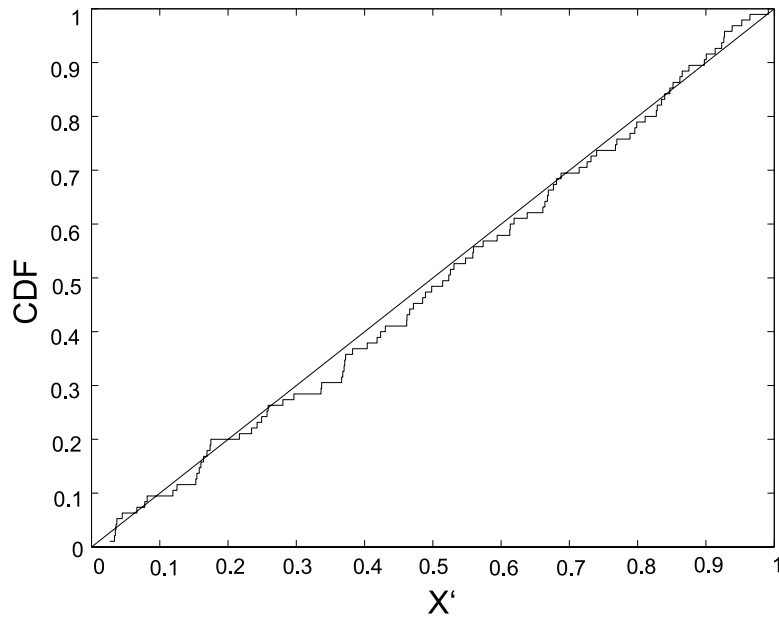


Fig. 8. Cumulative distribution function (CDF) of the relative positions x and x' of tiny wiggles within the polarity events respectively before (a) and after the rejection of a “blind” zone of ~ 10 km at both ends of the chron (b).

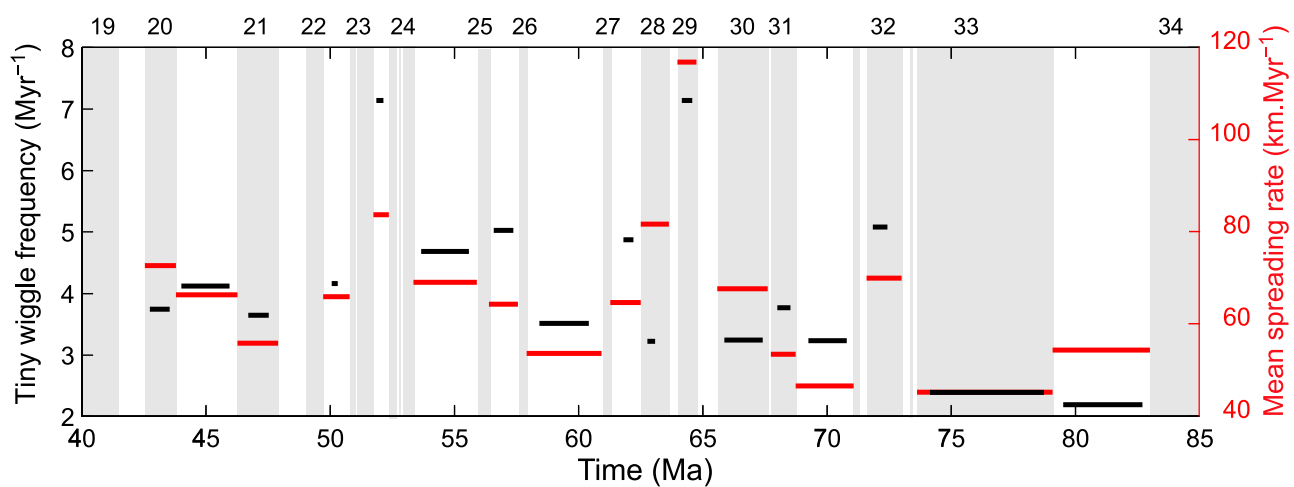


Fig. 9. Frequency of tiny-wiggles within each chron (in black) and mean spreading rate (in red) computed using the high resolution stack. Chrons having less than two tiny wiggles are not shown. The black bars are shorter than the chron durations because our frequency estimates were performed between the first and last tiny wiggles in order to exclude the “blind” period at both ends of chrons.

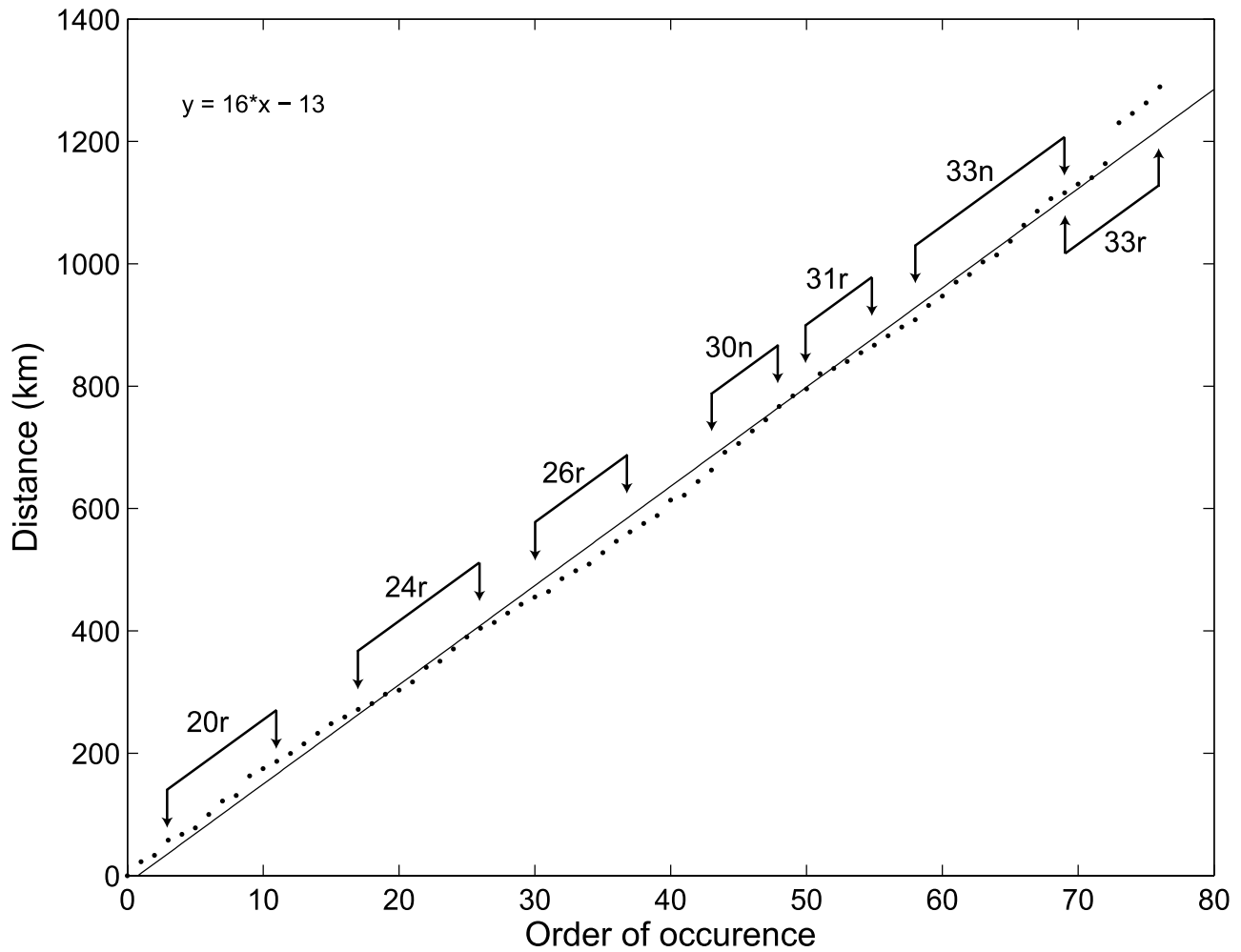


Fig. 10. Distance as a function of the order of occurrence of each tiny wiggle in a fictitious timescale that excludes the time intervals bounded by two tiny wiggles and containing a reversal. The dots define a straight line yielding a constant mean distance of ~ 16 km between successive tiny wiggles. The name of the longer chrons are reported for reference.

(a)

Area	Spreading direction (deg)	Skewness (deg)
1	N 0	80
2	N 5	80
3	N 210	-30
4	N 218	-35
5	N 180	-70

(b)

Area	Spreading direction (deg)	Skewness (deg)
6	N 180	80
7	N 252	40
8	N 260	40
9	N 260	60
10	N 260	80

(c)

Area	Spreading direction (deg)	Skewness (deg)
11	N 340	25
12	N 320	30
13	N 320	30
14	N 128	0
15	N 279	15
16	N 340	20

Table 1: Spreading directions and skewness corrections applied to profiles in the Indian (a), North Pacific (b) and South Pacific (c) oceans.

Chron	HR areas	MR areas	Stacks consistency	Number of tiny wiggles
19r	8-10		Area 10 consistent with area 8 but not with area 9	1 (a)
20n	8-10	7	good	4 (a,b,c,e), possibly 5 (d)
20r	8-10	1,5,7,15	good (except area 5 characterised by low anomalies amplitude)	9 (a-i)
21n	8-10	1,4,5,7,15	good	4 (a-d)
21r			poor (poor resolution and varying shape between the stacks)	0
22r	1,3,4,5	2,8-10	good (especially between area 1 and 4 which include a large amount of data)	3 (b-d), possibly 4 (a)
23r	1-5	8-10,15	good	3 (a-c)
24r	1-5,6,15	7-14,16	good	10 (a-j)
25r	1-5,15		good (except area 15)	5 (a,b,d-f), possibly 6 (c)
26r	1-5,15	7-14,16	good in fast spreading rate areas, lower in slow spreading rate	8 (a-h), possibly 9 (i)
27r	1-5		good (except for younger part, lower resolution of areas 2-4)	3 (c-e), possibly 5 (a,b)
28n	1-5		good (except area 4)	2 (a,b), possibly 3 (c)
29n	1-5		good (except area 4)	3 (b,c,e), possibly 5 (a,d)
29r	1,3,4,5		poor	0
30n	1,3,5,13	6-12,14	good	6 (a-f)
31n	1,3,5		good	3 (a-c)
31r	1,5,13	6-12,14	good (especially between areas 1, 5 and 13)	7 (a-g)
32n.2n	5,6,13,14	1,3,7-10	good (except area 6, poor resolution)	4 (a-d)
33n	1,3,5,7-14	6	partly consistent	12 (a-j,B,C)
33r	13	1,3,7-12,14	partly consistent	at least 2 (a,b)

Table 2: Description and comparison of the regional stacks for each chron, with the list of areas where the spreading rate allows a high (HR) or medium (MR) resolution record of the geomagnetic field fluctuations. We summarize the stack consistency with the other stacks and the number of identified tiny wiggles.

Interval (Ma)	Name	Interval (Ma)	Name	Interval (Ma)	Name			
41.888	41.892	C19r-1	55.577	55.583	C24r-10	68.525	68.535	C31n-3
42.737	42.743	C20n-1	56.579	56.581	C25r-1	69.245	69.255	C31r-1
43.045	43.055	C20n-2	56.720	56.724	C25r-2	69.782	69.797	C31r-2
43.198	43.202	C20n-3	56.955	56.965	C25r-3	69.962	69.977	C31r-3
43.535	43.545	C20n-4	57.187	57.193	C25r-4	70.212	70.227	C31r-4
44.007	44.013	C20r-1	57.373	57.377	C25r-5	70.527	70.533	C31r-5
44.147	44.153	C20r-2	58.415	58.425	C26r-1	70.793	70.797	C31r-6
44.307	44.313	C20r-3	58.585	58.595	C26r-2	71.830	71.850	C32n.2-1
44.636	44.644	C20r-4	58.975	58.985	C26r-3	72.046	72.054	C32n.2-2
44.964	44.976	C20r-5	59.212	59.228	C26r-4	72.258	72.262	C32n.2-3
45.103	45.117	C20r-6	59.415	59.425	C26r-5	72.428	72.432	C32n.2-4
45.586	45.594	C20r-7	59.767	59.773	C26r-6	74.138	74.142	C33n-1
45.767	45.773	C20r-8	60.117	60.123	C26r-7	74.658	74.662	C33n-2
45.947	45.953	C20r-9	60.407	60.413	C26r-8	74.987	74.993	C33n-3
46.699	46.701	C21n-1	61.796	61.804	C27r-1	75.486	75.504	C33n-4
46.929	46.931	C21n-2	62.008	62.012	C27r-2	75.778	75.782	C33n-5
47.209	47.211	C21n-3	62.206	62.214	C27r-3	76.226	76.234	C33n-6
47.520	47.524	C21n-4	62.765	62.775	C28n-1	76.489	76.491	C33n-7
50.053	50.067	C22r-1	63.076	63.084	C28n-2	76.981	76.999	C33n-8
50.299	50.301	C22r-2	63.784	63.810	C28r-1	77.565	77.575	C33n-9
51.857	51.863	C23r-1	64.148	64.152	C29n-1	78.068	78.072	C33n-10
51.987	51.993	C23r-2	64.215	64.225	C29n-2	78.528	78.532	C33n-11
52.136	52.144	C23r-3	64.401	64.419	C29n-3	78.728	78.732	C33n-12
53.655	53.665	C24r-1	64.564	64.576	C29n-4	79.506	79.514	C33r-1
53.797	53.803	C24r-2	65.866	65.874	C30n-1	79.778	79.782	C33r-2
54.011	54.019	C24r-3	66.295	66.305	C30n-2	79.967	79.973	C33r-3
54.107	54.113	C24r-4	66.500	66.520	C30n-3	80.385	80.395	C33r-4
54.309	54.311	C24r-5	66.810	66.830	C30n-4	81.612	81.628	C33r-5
54.643	54.657	C24r-6	67.085	67.095	C30n-5	81.896	81.904	C33r-6
54.795	54.805	C24r-7	67.408	67.413	C30n-6	82.217	82.223	C33r-7
55.088	55.092	C24r-8	67.995	68.005	C31n-1	82.695	82.705	C33r-8
55.365	55.375	C24r-9	68.315	68.325	C31n-2			

Table 3: Cryptochrons found in our study from chron 19r to chron 33r. Names follow the convention of Cande and Kent [7,6].